

Towards direct imaging and orbital parameter estimation of supermassive black hole binaries with spaceborne VLBI

B. Hudson^{1,★}, L.I. Gurvits^{1,2}, E. Mooij¹, A. Ricarte^{3,4}, and D. Palumbo^{3,4}

¹ Faculty of Aerospace Engineering, Delft University of Technology, Kluyverweg 1, 2629 HS Delft, The Netherlands

² Joint Institute for VLBI ERIC (JIVE), Oude Hoogeveensedijk 4, 7991 PD Dwingeloo, The Netherlands

³ Black Hole Initiative at Harvard University, 20 Garden Street, Cambridge, MA 02138, USA

⁴ Center for Astrophysics | Harvard & Smithsonian, 60 Garden Street, Cambridge, MA 02138, USA

November 12, 2025

ABSTRACT

Direct electromagnetic observation of the orbital motion of a sub-parsec, supermassive black hole binary (SMBHB) would provide the first conclusive proof of such systems existing. Widely considered to be the sources of gravitational waves, binaries are expected to form as a natural consequence of galactic mergers and determining the processes that drive their evolution is essential for understanding cosmological evolution. In this work, we evaluate the prospects of using ground and spaceborne Very Long Baseline Interferometry (VLBI) to observe supermassive black hole binaries and estimate their orbital parameters. The Black Hole Explorer (BHEX) is considered as the primary case study. Achieving unprecedented resolution, BHEX will provide access to a new volume of binary parameter space, potentially enabling the first, confident detection of an SMBHB. A binary toy model using a post-Newtonian orbit propagation is developed and simulated observations by BHEX and a ground array of telescopes are performed. An orbit fitting approach using Bayesian dynamic nested sampling is presented and its efficacy is demonstrated on the simulated observational data for a set of example binary systems. It is found that for BHEX, binary detection requires a total flux density of 0.04 Jy with a minimum separation of $\sim 2 \mu\text{as}$ and an observable mass ratio dependent on the total flux. With three annual observations, BHEX could constrain semi-major axis and eccentricity of binaries with orbital periods ≤ 10 years to within 13% of the true values. A curved trajectory could confidently be detected in binaries with period ≤ 23 years. Proposals for how candidate sources could be identified in time for the BHEX mission are also provided. Finally, we constrain the requirements of a future spaceborne VLBI system, capable of performing a statistically significant survey of supermassive black hole binaries.

Key words. instrumentation: interferometers – astrometry – quasars: supermassive black holes – submillimeter: galaxies – celestial mechanics

1. Introduction

Galactic mergers are inevitable in the course of the evolution of the Universe and supermassive black hole binaries (SMBHBs) are expected to form as a natural consequence of such mergers (Kormendy & Ho 2013, and references therein). Determining the processes involved in their formation and evolution is essential for understanding cosmological evolution on a galactic scale.

The stages of an SMBHB’s lifecycle (formation, inspiral, merger and ringdown) are defined in the pivotal work by Begelman et al. (1980). Following a galaxy merger, dynamical friction is capable of driving the binaries closer together (Callegari et al. 2011; Mayer 2013; Dosopoulou & Antonini 2017). Dynamical friction becomes inefficient at continuing to decay the binary orbit at a separation on the order of parsecs, in a process known as *hardening* (Merritt & Milosavljević 2005). Further evolution of an SMBHB may be driven by processes such as torque imparted on the binary due to interaction with a circumbinary gas disk (see Tang et al. (2017) and references therein) and/or asymmetric stellar distributions that promote a high interaction rate between the binary and surrounding stars (Gualandris et al. 2017). The final decay is controlled by dissipation of the binary’s kinetic energy via gravitational wave (GW) emission (Begelman et al. 1980; Merritt & Milosavljević 2005). In these stages of the

evolution, the separation between the SMBHB components decreases from single-digit parsecs to $\lesssim 0.01$ pc. A recent work by Gurvits et al. (2025) presents a model describing this evolution of an SMBHB towards coalescence and ring-down. Characteristic angular separations of components at these stages of evolution are of the order of $1 \mu\text{as}$ and smaller.

At the time of writing there has been no conclusive, direct evidence for the existence of sub-parsec SMBHB systems in electromagnetic (EM) observations. As described by D’Orazio et al. (2024), directly resolving a binary of this type through Very Long Baseline Interferometry (VLBI) is the only way to provide the desired, unambiguous evidence. However, the angular resolution required for such a detection (and subsequent imaging) is, in the best case, near the fundamental limit of ground VLBI systems. Even the “sharpest” ground-based VLBI system, the next generation Event Horizon Telescope (ngEHT), will have angular resolution no finer than $\sim 15 \mu\text{as}$ (Doeleman et al. 2023; Ayzenberg et al. 2025). D’Orazio & Loeb (2018) predict that with the capabilities of the ngEHT, a few SMBHB systems may be resolvable out to $z \lesssim 0.2$. From detection of the GW background, sub-pc binaries must exist as the measurements favour models with efficient merging instead of indicating the existence of a significant final-pc problem (Agazie et al. 2023).

Ground VLBI systems are fundamentally limited in angular resolution by the Earth diameter ($\sim 12,000$ km) and the highest

* e-mail: b.hudson@tudelft.nl

radio frequency (~ 345 GHz) permitted by atmospheric opacity. Thus a robust and statistically significant investigation of multiple SMBHB objects necessitates the use of space VLBI systems, which are free of these limitations.

Characterisation of a population of binaries would enable evolutionary models to be constrained across the SMBHB lifecycle. Multi-messenger studies, combining VLBI with EM observations at other wavelengths and GW observations, would enormously broaden the view on the evolution of galaxy constituents of the Universe. Resolving a population of SMBHBs would also improve predictions for the stochastic GW background, breaking model degeneracies (Agazie et al. 2023).

In this paper we consider the near-future prospects for direct, resolving observations of SMBHBs with spaceborne VLBI. A motivation for this work is driven by the prospect of synergistic studies of SMBHBs in both their EM and GW emission, the latter by the Laser Interferometer Space Antenna (LISA) mission (Colpi et al. 2024), Pulsar Timing Arrays (PTAs) (Agarwal et al. 2025) and other, future GW facilities.

Two concepts of spaceborne VLBI are used as case studies. The first, the Black Hole Explorer (BHEX) is a proposed, 2-year extension to ground-based arrays such as the EHT, aiming to detect a black hole's photon ring with an angular resolution of $\sim 6 \mu\text{as}$. On baselines with ALMA, BHEX will achieve a sensitivity of $\sim 1 \text{ mJy}$ (Johnson et al. 2024; Hudson et al. 2023). We also consider the TeraHertz Exploration and Zooming-In for Astrophysics (THEZA) concept, originally prepared in response to the European Space Agency's (ESA) call for its science program Voyage 2050 (Gurvits et al. 2021, 2022). We define high-level requirements for a THEZA-like system to perform a more expansive SMBHB survey with an angular resolution on the order of $1 \mu\text{as}$.

Direct detection of orbital motion in SMBHBs at sub-parsec scales would provide a novel test of GR in the strong-field regime where the orbital velocities are approaching a significant fraction of the speed of light. Post-Newtonian effects such as periastron precession, spin-spin and spin-orbit coupling could be observed with multiple observations of the same system over time (Gergely & Biermann 2009, and references therein). Black hole spin can be estimated through its correlation with the spiral pitch angle of the linear polarisation pattern (Palumbo et al. 2020; Chael et al. 2023; Palumbo 2025; Wong et al. 2025; Hou et al. 2025) and this would provide constraints for modelling spin evolution during accretion and binary inspiral (Sayeb et al. 2021; Ricarte et al. 2023; Sala et al. 2024; Ricarte et al. 2025). Spin measurements with an accuracy of 10% are expected to come from the photon ring measurements of M87* and Sgr A* made by BHEX (Johnson et al. 2024).

Ayzenberg et al. (2025) discuss the different types of binaries in the context of their detectability with VLBI. We consider the case of a telescopic or visual binary where both components are detected and the angular resolution is at least of the order of the binary separation. Only an observation of a telescopic binary would provide direct evidence of a sub-parsec SMBHB.

In this paper, we propose a methodology for the two objectives discussed above, namely, VLBI detection of an SMBHB and monitoring of its orbital motion using a Bayesian inference and post-Newtonian orbit fitting technique. In doing so, we provide an approach that could be used for future SMBHB VLBI observations. This technique is also used to determine the likelihood of a mission such as BHEX being able to accurately constrain orbital parameters and for defining preliminary requirements of a future spaceborne VLBI system such as THEZA.

In Section 2, the orbit fitting approach is presented. In Section 3, an evaluation of the binary observation prospects of BHEX are discussed, along with synthetic data simulations and demonstration of the orbit fitting methodology. Finally, in Section 4, preliminary requirements of a future spaceborne VLBI mission to perform imaging SMBHB surveys are defined.

2. Method

For orbital parameter estimation, the interferometer should be capable of observing the SMBHB candidate over a protracted time period. The method developed here could also be applied to an astrometric binary, where the proper motion of one component is detected with respect to some reference source, if future astrometry provides precision on the order of that discussed by Zhao et al. (2024).

The analysis pipeline presented requires a sample of relative right ascension and declination positions of the secondary black hole with respect to the primary. Other observables such as: the flux density of the sources over time; whether the black hole components have been resolved on an event horizon-scale; and redshift estimates, also play a key role in this methodology.

From the relative position data, the process is then divided into two phases: binary *confirmation* and orbit *estimation*. The former involves building confidence that what is being observed is two SMBHB exhibiting non-linear, relative motion. For the latter, sufficient observations of the system over time have been performed to constrain its orbital parameters.

2.1. Binary Orbit Model

For simulating VLBI observations of SMBHBs and for calculation of the likelihood of candidate orbits in the Bayesian fitting process, a post-Newtonian, (PN) binary orbital model has been implemented. The model is based upon that described by Blanchet (2024) up to order 3.5PN. This is consistent with the typical consideration for massive black hole inspirals (e.g., Piarulli et al. 2025, and references therein). The rationale behind excluding higher order effects is discussed below. The acceleration function is defined as

$$\ddot{\mathbf{x}} = -\frac{GM}{r^2}[(1 + \mathcal{A})\mathbf{n} + \mathcal{B}\mathbf{v}] \quad (1)$$

where $M = m_1 + m_2$, $\mathbf{n} = \mathbf{x}/r$ and the orbital separation is $r = |\mathbf{x}|$. The coefficients \mathcal{A} and \mathcal{B} , which describe the PN perturbations in increasing powers of c , are provided by Pati & Will (2002). Acceleration is calculated in the centre-of-mass frame, and the black hole positions are

$$\mathbf{x}_1 = \frac{m_2 \mathbf{x}}{M} \text{ and } \mathbf{x}_2 = \frac{-m_1 \mathbf{x}}{M} \quad (2)$$

The acceleration function is integrated from a set of initial Campbell orbital elements defined as: semi-major axis (a), eccentricity (e), inclination (i), position angle of nodes (Ω), argument of periastron (ω) and time of periastron passage (T_0). An explicit, 8th order Runge-Kutta method is used for the integration. As described by Blunt et al. (2017), for orbit fitting the parameter τ is used instead of T_0 as the prior bounds for it are simply between 0 and 1, regardless of orbital period. T_0 is related to τ by

$$\tau = \frac{T_0 - t_{\text{ref}}}{P_{\text{rest}}} \quad (3)$$

where t_{ref} is some specified reference date and P_{rest} is the rest-frame orbital period, all in the same time units (e.g., Modified Julian Date).

Other, higher-order effects exist in PN propagation that have not been implemented for this preliminary formulation of the pipeline. Provided in Appendix A is an evaluation of the order of magnitude effect of these additional perturbations and justification for their inclusion/exclusion. In summary, Schwarzschild black holes are considered with zero spin. Thus, the spin-spin, spin-orbit coupling effects described in Dey et al. (2018) are not included. Nor are the other terms in \mathcal{A} and \mathcal{B} beyond 3.5 PN.

However, the effect of the relative light travel time from each source is taken into account. Although they will be observed on a flat sky plane, any orbit that is not face-on will have one black hole further from the observer. The time taken for this extra distance to be traversed by the emission is non-negligible and will result in the farther black hole's position being from an earlier time relative to the other source. Details of how this has been modelled are provided in Appendix A.

2.2. Binary Confirmation

Upon observing a binary candidate with a VLBI array, a challenge will be how to gain confidence that what has been measured is indeed an interferometric response to an SMBHB structure. With the likely faintness and small angular separation of the two sources, it is conceivable that the points of emission may not be gravitationally bound and what is being observed is two independent sources with close celestial positions or a combination of an AGN core and a jet. Other scenarios for potential false alarms can also be imagined. Confirming a binary detection will require evidence to reject these null hypotheses. This evidence can be considered in two categories:

1. Are the sources supermassive black holes?

For most sources of future VLBI observations of binary candidates, they will appear as unresolved and point-like or Gaussian due to the very high angular resolution required to resolve them on an event horizon (EHT-like) scale. Observational features that will provide strong evidence of the sources being black holes include: the launching of relativistic jets; spectra showing flux density rising with frequency suggesting compact, non-thermal emission; location within the centre of a known AGN and evidence from multi-wavelength observations. If one or both of the sources have their shadow resolved then this in itself is direct evidence.

2. Are the sources exhibiting orbital motion?

Confirming an SMBHB detection requires observing orbital motion. It is the process of observing and constraining this motion that the rest of this section is focused on.

We consider linear motion as the null hypothesis to be rejected in the attempt to detect orbital motion. This is based upon the assumption that if the objects are not gravitationally bound, they are most likely to be exhibiting linear motion on the small angular diameter scales a VLBI mission would probe. Sources on much larger orbital paths which could be the source of erroneous binary detections would likely appear as linear motion on these scales. Other potential sources of erroneous binary detection could be bright components in a relativistic jet exhibiting

some relative motion on short timescales. In such cases, where it is feasible that relative motion may be non-linear, the other forms of evidence listed above would have to be carefully considered along with the goodness of fit of an orbit, determined using this approach.

A useful metric for planning future VLBI missions is the number of observations required to confidently detect curvature in the observed motion. This expression is based on the need for the curvature in the trajectory to exceed the noise in the measurements. For an inclined, circular orbit, the number of observations required N_{min} is

$$N_{\text{min}} = \max \left(3, \left\lceil 1 + \sqrt{\frac{k\sigma_{\text{pos}} P_{\text{obs}}^2}{a\pi^2 t_{\text{cad}}^2 \cos i}} \right\rceil \right) \quad (4)$$

where P_{obs} is the observed binary orbital period ($P_{\text{obs}} = (1 + z)P_{\text{rest}}$), t_{cad} is the cadence of observations and a is the orbit semi-major axis. σ_{pos} is the uncertainty on the position estimation. Appendix B contains the full derivation of this analytic expression. The position angle of nodes does not enter the equation as its rotation does not affect the curvature of the orbit, only the orientation of the ellipse on the sky plane. Fig. 1 depicts N_{min} for a circular, face-on orbit of varying semi-major axis and orbital period. Representative performance values for BHEX and the ngEHT have been used. An estimate for σ_{pos} is calculated using the expression from Rioja & Dodson (2020)

$$\sigma_{\text{pos}} \approx \frac{\theta_r}{\text{SNR}} \quad (5)$$

where Signal-Noise Ratio (SNR) for both interferometers is calculated for a source with $F_{\nu,\text{tot}} = 0.05$ Jy and assuming an average sensitivity of 4 mJy (determined from the BHEX simulations presented in Section 3). However, the astrometric precision is further improved inversely proportional to $\sim \sqrt{N_{\text{base}}}$ where N_{base} is the number of independent baselines given by $N_{\text{base}} = \frac{N_A(N_A-1)}{2}$ and N_A is the number of antenna in the array. This effect has been included in the generation of Fig. 1. In the synthetic data simulations presented below we find that the number of scans at a given time does not significantly affect the astrometric precision.

For the source total flux density and sensitivity assumed above, the independent sampling by multiple baselines reduces σ_{pos} from 0.48 to 0.09 and this is demonstrated with the results presented in Section 3. The perhaps surprising degree of accuracy with which the source positions can be estimated results in the ability for BHEX, ngEHT or a future THEZA system to confidently reject the possibility of linear relative motion for very long period orbits with only a few observations. However, the actual orbit fit accuracy will reduce as the orbit period increases for the same N_{min} . This will be further demonstrated with synthetic data simulations in Section 3.

Extending this approach to elliptical orbits, as part of the Bayesian orbit fitting approach, the False Alarm Rate (FAR) of the Maximum A Posteriori (MAP) solution is calculated. This FAR represents the probability that the apparent orbit motion signature could simply arise from noise in a linear trajectory. A two-parameter linear model is fitted to the data (gradient and intercept in the $(\Delta\alpha)$ and $(\Delta\delta)$ system). The FAR is then calculated using a chi-squared test.

2.3. Orbit Estimation

Once sufficient observations of a source have been performed to gain confidence that it is a likely binary candidate, the or-

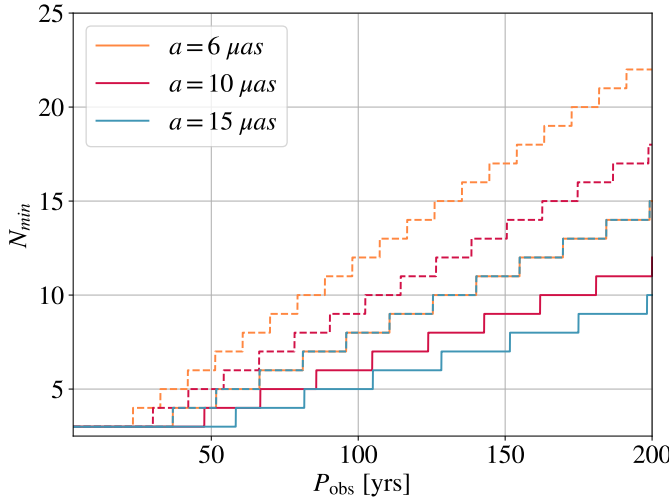


Fig. 1. Minimum number of observations required to detect curved motion of secondary black hole as a function of observed orbital period and semi-major axis in angular units. Face-on orbit with no inclination. Observations performed annually. (Solid lines) BHEX with angular resolution of $6 \mu\text{as}$. (Dashed lines) ngEHT with angular resolution of $15 \mu\text{as}$.

bital parameters can be estimated. Fang & Yang (2022) present a Newtonian orbit fitting approach for a binary model consisting of two point sources. They demonstrate how the orbital parameters can be determined directly from the visibility data. Here we present an extended method, consisting of a PN orbit model and one that is applicable to various forms of binary models (i.e., not just point sources) and can also be used on reconstructed images.

The group of Bayesian Markov Chain Monte Carlo (MCMC) methods is widely used in astronomy for orbital parameter estimation across a diverse range of disciplines from stellar binaries to exoplanets (Pearce et al. 2020; Blunt et al. 2017). Other algorithms such as the Least Squares Monte Carlo (LSMC) method or more traditional orbit fitting (e.g., Gauss's and Gibbs methods, Lambert's problem) are effective at finding only the best fit solution, under specific, required conditions for the number of and cadence of observations.

However, as noted by Thompson et al. (2023), it is challenging to compute posteriors for traditional orbital elements as they consist of complex co-dependencies and degeneracies. This is exacerbated when working with short orbital arcs, as is likely to be the case for SMBHB observations. Depending on the type of MCMC method used, they can be ineffective at estimating the posterior for highly multi-modal problems. Variants such as the parallel-tempered method used by Blunt et al. (2017) aim to address this issue.

Dynamic nested sampling has been shown to be effective at estimating Bayesian posteriors in an astronomical context, particularly when compared to MCMC methods (Speagle 2020). Dynamic nested sampling adaptively allocates samples depending on the posterior structure, enabling it to effectively sample multi-modal distributions. For this orbit fitting approach, we have implemented the dynamic nested sampling Python package *dynesty*¹ (Speagle 2020).

A custom, Gaussian log-likelihood function is used as the positional uncertainties are primarily driven by thermal noise which is Gaussian in nature. This takes the form

$$\log \mathcal{L}(\mathcal{D} | m) = -\frac{1}{2} \sum_{i=1}^{N_{\text{obs}}} \frac{(\Delta\alpha_{\text{obs},n} - \Delta\alpha_{m,n})^2}{\sigma_{\text{pos},n}^2} + \frac{(\Delta\delta_{\text{obs},n} - \Delta\delta_{m,n})^2}{\sigma_{\text{pos},n}^2} \quad (6)$$

where the subscript obs, n are the observed positions of the n^{th} observation and m, n are the positions calculated from the trial model parameters using the PN orbit model. N_{obs} is the number of observations. A prior transform is used that only allows physically realistic values of the orbital parameters and black hole masses, this is discussed in section 2.4.

The orbit fitting calculates the optimum values of the following parameters to fit the observational data: total mass M , mass ratio $q = \frac{m_2}{m_1}$, a , e , i , Ω , ω and τ . The tuneable parameters of *dynesty* have been determined through preliminary runs of the test cases presented below. We use the random walk sampling method and multiple ellipsoid bounding, as is suggested for multi-modal distributions. For live points, Speagle (2020) suggests 50 times the number of degrees of freedom, for each expected mode. Through preliminary tests, increasing the value of `nlive_init` beyond 12000 produced minimal change in already smooth and well-sampled posterior contours, and therefore this value was used for all cases. The `dlogz` tolerance, the stopping condition for the initial baseline run, is set to 0.005.

2.4. Parameter Constraints

dynesty draws samples from a prior transform function, within which constraints can be applied to the parameters based on other observational data or prior knowledge of the source. This can increase the rate of convergence to a best fitting solution whilst ensuring only physically realistic values are sampled. Care should also be taken to ensure that the parameter search space is not artificially limited.

An upper limit can be applied to the black hole mass ranges based on whether the two binary components have been resolved in the VLBI observations. The diameter of a resolved black hole shadow is related to its mass m by

$$\theta_s \approx \frac{2\sqrt{27}Gm}{c^2 D_A} \quad (7)$$

where D_A is the angular diameter distance which can be calculated from knowledge of the source's redshift (Bardeen 1973). Redshift can be measured from other observations of the host galaxy's emission or absorption lines. As such, even if the shadow is not resolved, this expression provides an upper limit on the black hole mass. A lower limit can be estimated from SED models of such systems (see Pesce et al. (2021)) and the fact that the source has been detected in the first place. Scaling relations between the black hole and host galaxy will also be useful for determining the likely lower limit. For the subsequent example cases, it is assumed that the total black hole mass is known to within an order of magnitude of solar masses.

Semi-major axis can be constrained from measurement of the angular separation of the binary across different observations. Assuming a near face-on orbit with little inclination, the maximum semi-major axis can be determined by assuming a highly elliptical orbit and that the observed black holes are currently at periastron.

$$a_{\text{max}} = \frac{r_{\text{sep}}}{1 - e} \quad (8)$$

¹ <https://github.com/joshspeagle/dynesty>

For an inclined orbit, the observed separation is a function of the semi-major axis and the inclination. In the worst-case, a binary may be viewed completely edge on ($i = \frac{\pi}{2}$) with the black holes almost aligned. The observed instantaneous separation would then be a tiny fraction of the true semi-major axis. From multiple observations (as would be required to perform orbit determination), constraints will be able to be applied to the semi-major axis. The prior imposed on a ranges from 0.001 pc to twice the true semi-major axis.

Eccentricity is allowed to vary between 0 and 1, permitting only elliptical orbits to be included in the orbit fitting. Although hyperbolic orbits where the black holes are not yet fully bound are theoretically possible, they are far less likely on the small angular scales being probed with VLBI. It is also less probable to observe such a system, given how little time it would spend in such a state, when considered on cosmological timescales.

The angular orbital elements are allowed to vary within their full range in the subsequent examples. The position angle of nodes (Ω) and argument of periastron (ω) range from 0 to 2π whilst inclination (i) varies between 0 and π . The epoch of periastron passage (τ) is allowed to vary between 0 and 1, as described in the previous section. We present angular parameter results in degrees for ease of comprehension.

An additional constraint that is not yet included in the orbit fitting approach is variation in the observed flux density of the source. For an inclined orbit, the relativistic Doppler shift will vary across the orbit causing time-varying redshift modulation. Measuring this Doppler effect would provide information on the direction of motion of each black hole at a given time and thus the inclination of the orbit. D’Orazio et al. (2015) discuss variable Doppler boosted emission as the source of the variability observed in PG1302-102. The potential difficulty in using such a constraint is identifying Doppler boosted emission from intrinsic variability of the source.

3. Prospects of SMBHB detection with BHEX

The Black Hole Explorer (BHEX) is a sub-millimetre, space-borne VLBI concept, currently in development, and intended for submission to NASA’s Small Explorers (SMEX) programme at the next call for proposals (Johnson et al. 2024). If accepted, BHEX will detect a black hole’s photon ring for the first time. The supermassive black holes M87* and Sgr A*, the horizon-scale targets of the EHT, are the primary sources for photon ring detection (Event Horizon Telescope Collaboration et al. 2019, 2022).

Binary observation has been identified as a potential activity of the ngEHT (Ayzenberg et al. 2025). As shown in Fig. 2, D’Orazio & Loeb (2018) predict a small number of binary systems may be observable with the ngEHT. It should be noted that the model developed by D’Orazio & Loeb (2018) should be revisited given the recent GW background measurements by the NANOGrav collaboration. Agazie et al. (2023) find a strain amplitude of $2.4^{+0.7}_{-0.6} \times 10^{15}$ for a frequency of 1 year^{-1} . In Fig. 2 of D’Orazio & Loeb (2018), they present the predicted GW background from their model. For the same frequency, the strain amplitude broadly agrees with the PTA measurements. A more thorough examination of the assumptions made should be performed but this preliminary evaluation suggests that the model used to estimate the number of observable sources broadly agrees with the measured GW background.

Providing baselines with ground antenna exceeding 20,000 km, BHEX will achieve an angular resolution of $\sim 6 \mu\text{as}$. This improvement on current capabilities warrants evaluation

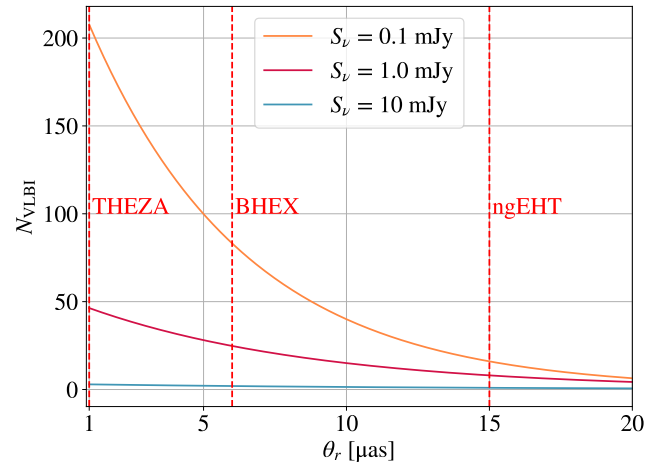


Fig. 2. Predicted number of observable SMBHB systems as a function of array angular resolution (θ_r) and flux density sensitivity (S_v) out to $z = 2$. $P_{\text{obs}} \leq 10$ years and $q \geq 0.01$. Figure generated using the assumptions made by D’Orazio & Loeb (2018) in the generation of their results.

of the binary detection prospects of the system. The primary advantage of adding BHEX to the array is the finer resolution. This will increase the number of resolvable systems and provide beneficial sampling of the (u, v) plane on long baselines. The inclusion of BHEX observations increases the likelihood that a confident first binary detection will be performed in the near future with VLBI.

3.1. Binary Detection

As an interferometer, BHEX and a ground array of telescopes samples the complex visibility of a target source - the noise-corrupted Fourier transform of its true image. Detecting a binary first requires discerning two distinct sources in the visibility data. Fig. 3 shows the observable region of binaries by BHEX, as a function of flux density and solid angle ratio and separation between the primary and secondary components. If it is assumed that the flux density of the two black holes scales proportionally with their mass, the y-axis of this plot can be considered as the mass ratio (q). The figure depicts the required total flux density of the binary for BHEX to distinguish it from a single Gaussian source. A binary detection is defined as when the correlated flux density on BHEX baselines is 3σ discrepant from the total flux density and also from the flux density of the primary Gaussian source.

BHEX is able to detect binaries with a lower total flux density as the primary becomes more compact (moving from left to right in Fig. 3) and the separation increases. $F_{v,\text{tot}} = 0.5 \text{ Jy}$ is the approximate total flux density of M87*, the brightest horizon-scale source for ground VLBI observations. As such, the white regions of this figure depict parameter space where a total flux density greater than this is required to detect a binary. Therefore, it becomes increasingly less likely that such systems exist. Considering this constraint, BHEX is able to detect binaries with a mass ratio of $q \geq 0.045$, if it is assumed that the flux density scales proportionally to the black hole mass, and that sources with $F_{v,\text{tot}} = 0.5 \text{ Jy}$ can be found.

Assuming a thermal noise figure of 5 mJy, binaries with a total flux less than 0.04 Jy are not detectable, noting that the ther-

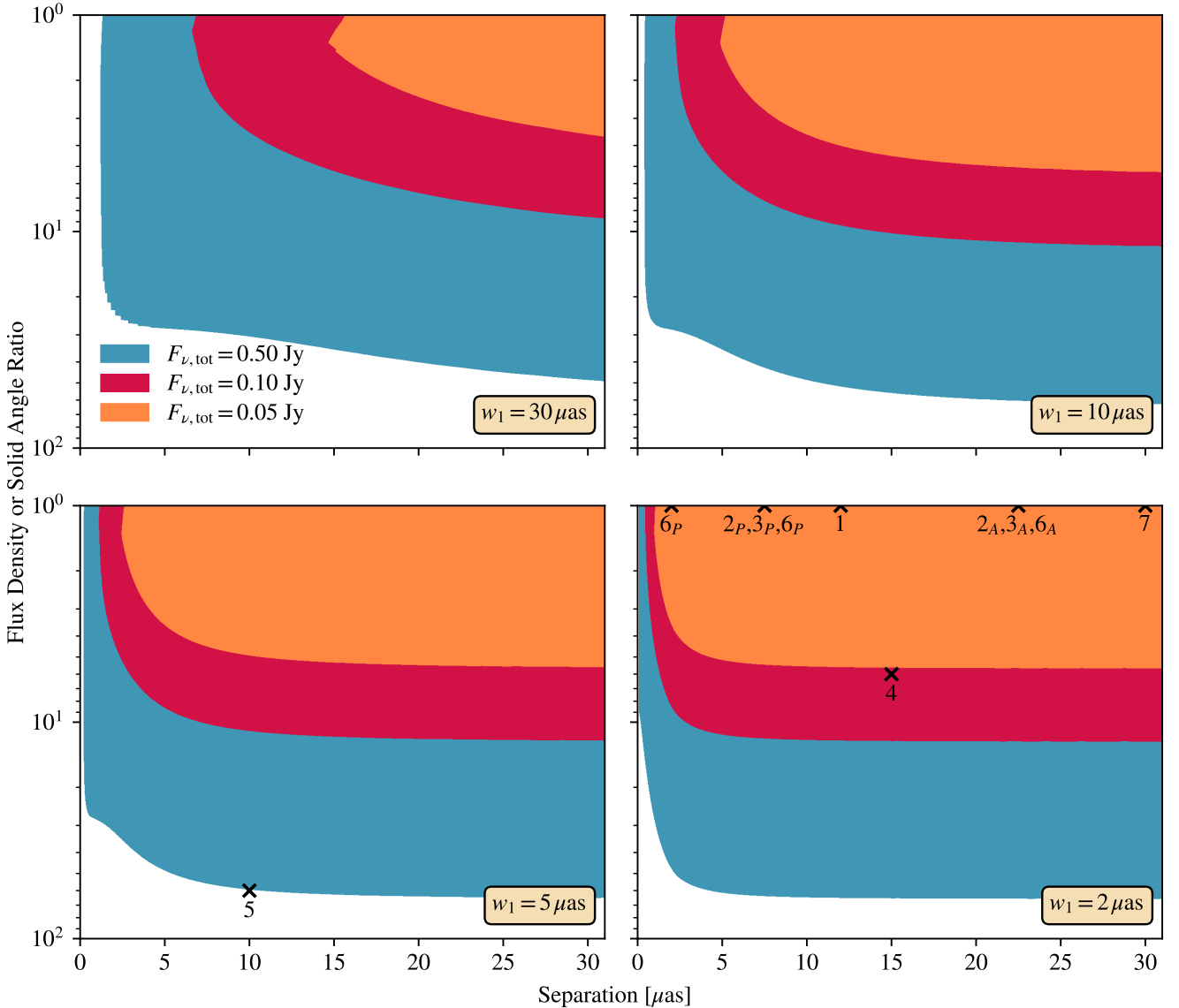


Fig. 3. BHEX capabilities of binary system detection. Depicts the total flux density of the source required to distinguish a binary from a single Gaussian source, assuming a brightness thermal noise of 5 mJy/beam. w_1 is the angular diameter of the primary black hole. The y-axis describes the ratio between the primary and secondary component flux densities and solid angles. For illustrative purposes, we assume the same brightness for both components of the binary system. The positions of the 7 test cases presented below are illustrated in this parameter space. Subscript A indicates the largest angular separation of the orbit from the observer's perspective and P is the smallest observed separation.

mal noise is dependent on the specific ground sites participating in the observation. In the best case (on baselines between BHEX and ALMA in a 10 minute scan, with a thermal noise of ~ 1 mJy), binaries with a total flux of ≥ 7 mJy are detectable, for a flux density/size ratio of 0.75. However, as has been found in GRMHD simulations of close binary systems, for low mass ratios the secondary may be more active than the primary (D’Orazio et al. 2013; Farris et al. 2014; D’Orazio et al. 2016). In such cases, the detectable mass ratio by BHEX could be greatly reduced to $q \sim 0.01$ for a range of total flux densities. BHEX can detect binaries with separations down to ~ 2 μ as, although these would be unresolved.

D’Orazio & Loeb (2018) predict that with BHEX and the full ground array, $\lesssim 50$ SMBHB systems with $P_{\text{obs}} \leq 10$ years would be observable. Furthermore, by positing a flat mass ra-

tio distribution, D’Orazio & Loeb (2018) find that the number of observable systems is skewed towards low mass ratios (i.e., $q \ll 1$). However, they note that increasing the maximum orbital period always results in more observable binaries, by an order of magnitude in the example they provide (we provide an example of such a case below as observing them is more probable than shorter period systems). As discussed above, the assumptions inherent in these estimates should be revisited given recent GW background measurements. The results from D’Orazio & Loeb (2018) do however demonstrate that binary detection is likely to be at the edge of the ngEHT’s and BHEX’s capabilities.

3.2. Simulated Observations

To demonstrate the orbit fitting approach and evaluate BHEX's efficacy at detecting binaries, simulated BHEX observations have been modelled using `eht-imaging`² (Chael et al. 2018) and `ngehtsim`³. The spacecraft and ground array positions are propagated across the simulation time and simulated VLBI observations are generated of a given image model. Impacting factors such as thermal noise, weather conditions, atmospheric effects and station-based gain variations are included in the model. `ngehtsim` provides the ability to model Frequency Phase Transfer (FPT) allowing the phase from a lower frequency observation to be transferred to the higher band to increase coherence time (Rioja et al. 2011; Pesce et al. 2024; Issaoun et al. 2025).

A binary toy image model has been generated, consisting of two, circular Gaussian sources and using the PN orbit propagation presented in Section 2.1. We note that this is a simple binary representation, with no contributions from jets launching from one or both black holes. To demonstrate the effectiveness of this analysis for different binary appearances, in Appendix C.2, examples of binaries with unequal masses and varying Gaussian characteristics are presented. We assume a flat spectrum of the sources for simplicity and because detection of such a system would be more difficult than one with a rising spectrum.

We use a total flux density of 0.05 Jy, in accordance with the limit of BHEX's ability presented in Fig. 3, for the upper and lower bands' combined total flux density of the sources. Fig. 4 depicts the toy binary model. To ensure the example sources are physically realistic, we calculate the brightness temperature T_b using

$$T_b = (1 + z) \frac{2 \ln(2) c^2}{\pi \nu^2 k \theta^2} F_{\nu, \text{tot}} \quad (9)$$

where θ is Full Width at Half Maximum (FWHM) and ν is the observational frequency. For the primary source used in the first three examples with $F_{\nu, \text{tot}} = 0.03$ Jy, $T_b = 9.4 \times 10^{10}$ K, within the typical brightness temperature range of VLBI sources.

BHEX is projected to use a 3.4 m antenna with a surface accuracy of $\sim 40 \mu\text{m}$. Observing at high (240 – 320 GHz) and low (80 – 106 GHz) frequency bands, and in two polarisations, BHEX will perform FPT to achieve longer integration times. See Appendix C.1 for a full definition of the ground array and other simulation configuration parameters.

In our previous work, the various *functional constraints* impacting a space-based VLBI mission were analysed with methods for mitigation proposed for BHEX's specific challenges (Hudson et al. 2025). The engineering concept for BHEX is not yet sufficiently defined to include such inefficiencies with any certainty. As such, the issues of data downlink limitations, radiator, star tracker blinding and other factors limiting (u, v) coverage, are not included in these simulations. The effect of Sun and Earth blinding of the main antenna are, however, modelled as these do not depend on the design of the spacecraft. For this model, BHEX is assumed to be operating in a polar, Medium Earth Orbit (MEO), at an altitude of ~ 26562 km. Justification for this orbit selection is given by Hudson et al. (2025). BHEX will observe with a cadence of every 1 hour, resulting in full azimuthal sampling of the (u, v) plane, across its ~ 12 hour orbit.

`eht-imaging` provides functionality for model fitting to VLBI data. The native `dynesty` dynamic nested sampling ap-

proach is used. In the subsequent example cases, model parameters for two Gaussian sources are fitted to the data from which are extracted the relative right ascension and declination positions of the secondary black hole. The visibility amplitudes and closure phases are the datasets used to assess likelihood. We also fit a single Gaussian source to the same data and evaluate the difference in the goodness of fit to assess the likelihood of a false detection of a binary.

3.3. Orbital Parameter Estimation

Using the binary toy model and simulation pipeline described previously, in this section the orbit fitting approach is demonstrated for three example binary configurations. The test case parameters are provided in Table 1. For all three, m_1 and m_2 are equal but the flux density is unevenly distributed between the components to break the degeneracy that exists in the visibility domain if the sources were exactly the same. It is unlikely that in a real observation the emission characteristics of the two components would be identical. Justification for each scenario is provided below. In all cases, the black holes are shown in the m_1 -centred frame as this is what is observed by the array. Eq. 2 can then be used to convert back to the barycentric frame which is in effect the true inertial motion of the objects.

1. Circular, face-on binary depicting the simplest orbit model. Separation is near the limit of BHEX resolution and a short P_{obs} to demonstrate a binary source for which a large percentage of the orbital period is sampled. Gaussian sources with FWHM diameters below BHEX resolution as is likely for a binary at redshift higher than M87* and Sgr A*.
2. Eccentric, face-on binary to demonstrate the effect of eccentricity on the orbit fitting. Periastron separation near the limit of BHEX resolution. Longer P_{obs} (for which observable systems are more likely to exist) to demonstrate uncertainty in fitting orbit to small, observed arc.
3. Eccentric, inclined binary to demonstrate the effect of inclination on the orbit fitting.

Also provided in Appendix C.2 is a summary of the results of additional binary observation simulations for other intriguing cases. Justification for their selection is provided in the appendix and the results are discussed in Section 4. Similar to Blunt et al. (2017), the small number of provided cases aims to explore as much of the detectable binary parameter space as possible, with a focus on the minimum and maximum of important parameters (e.g. total flux density, inclination, angular separation, orbit period), whilst staying within realistic limits for mass-luminosity relations.

In a nominal ~ 2 year mission, the first 1–2 months will be spent in a commissioning phase. For the subsequent examples, an observing cadence of $t_{\text{cad}} = 1$ year is assumed, beginning as soon as commissioning is complete with two subsequent observing sessions of the same source, during the M87* observation window. The source is observed for one night at each of these epochs. The mass ratio is also kept constant at $q = 1$ (unequal mass cases considered in Appendix C.2). The total mass M , redshift and specific orbital parameters have then been tuned to produce example cases with realistic mass-luminosity relations. A redshift of 0.05 is settled on and the resultant masses lie close to the fundamental plane of black hole accretion at millimetre wavelengths, discovered by Ruffa et al. (2023). The source is assumed to lie close to M87* on the sky.

For the visibility data model fitting, we fix the brighter of the Gaussian components to the origin. A flat prior is defined for the

² <https://github.com/achael/eht-imaging>

³ <https://github.com/Smithsonian/ngehtsim>

Table 1. Test case summary. For all cases, Ω , ω and τ are set to 0 as they are expected to have less impact on the orbit fitting than the varied parameters. χ^2_{amp} and χ^2_{cp} describe the average goodness of fit of the binary Gaussian model in amplitude and closure phase to the observed data in eht-imaging, across the three observation epochs. The subscript *sin* describes the χ^2 values for fitting a single Gaussian source to the observed data. χ^2_{orb} describes the goodness of fit of the MAP orbital solution.

Case	$F_{\nu,\text{tot}}$ [Jy]	q	P_{obs} [yr]	Separation [μas]	e [-]	i [$^\circ$]	M [$10^8 M_\odot$]	$\text{FWHM}_{1/2}$ [μas]
1	0.03/0.02	1	5	12	0	0	4.00	2/2
2	0.03/0.02	1	10	$r_p = 7.5, r_a = 22.5$	0.5	0	3.37	2/2
3	0.03/0.02	1	10	$r_p = 7.5, r_a = 22.5$	0.5	45	3.37	2/2
νL_ν [ergs $^{-1}$]	χ^2_{amp}	χ^2_{cp}	$\chi^2_{amp,sin}$	$\chi^2_{cp,sin}$	$\sigma_{\text{pos,av}}$ [μas]	χ^2_{orb}	FAR [%]	
1	$5.54/3.68 \times 10^{41}$	0.23	0.29	9.77	1.72	0.078	6.35	0
2	$5.54/3.68 \times 10^{41}$	0.15	0.31	3.13	0.39	0.17	5.97	0
3	$5.54/3.68 \times 10^{41}$	0.14	0.31	3.13	0.39	0.19	5.90	0

secondary component's position between $\pm 50 \mu\text{as}$. A flat prior is used for both component's total flux density and FWHM of 0–1 Jy and 0–30 μas , respectively. σ_{pos} is provided by the model fitting in eht-imaging.

3.3.1. Case 1: Circular, Minimum Separation

The Stokes I image of the binary model is shown in Fig. 4. Table 1 and 2 summarises the model and orbit fitting results. The true, median and MAP orbit parameters are provided in Table 2, along with relative errors where they can be calculated. Fig. 5 depicts the best-fit orbit. The low FAR supports the analytic prediction presented in Section 2.2. Additional, useful figures are provided in Appendix C.2, including, the posterior distribution corner plot.

As will be seen in all test cases, the small number of observations results in a highly multi-modal problem. However, important constraints can be pulled from the posteriors. Total mass M has a single, main mode and shows a relatively tight posterior distribution. As a large arc of the orbit has been sampled, the semi-major axis a and eccentricity e are very well constrained, with a clear tendency towards a circular orbit. Mass ratio q is degenerate without prior constraints on the mass distribution which we have not imposed. We also see the expected degeneracy between M and the angular parameters (i , Ω and ω) as the former controls the dynamical scale of the orbit and the latter the geometric projection on the sky. In particular, wide posteriors for Ω and ω are expected as for a circular orbit, they do not change the projected shape of the orbit. The effect of angle wrap-around and a 180° degeneracy in the parameters is also evident, this is discussed further in the next section. The posterior distribution suggests a low inclination, but in general it is poorly constrained. τ is showing some tendency towards 0 or 1 and this is expected as both describe the periastron position at which observations began. We see a broader posterior in τ compared to latter cases as for a truly circular orbit, the periastron position has no physical definition.

In general, the posterior shows a mostly circular, low-inclination orbit with a well-constrained dynamical scale but with strong degeneracies and multimodality in angular parameters.

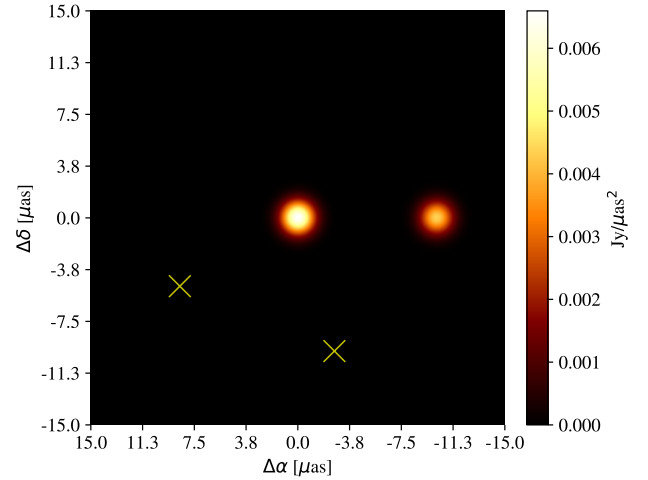


Fig. 4. Stokes I image of the binary toy model for Case 1 in Mar 2032, 2033, and 2034. Primary source fixed to origin and first position of secondary illustrated. Subsequent observed positions of secondary depicted with yellow crosses.

3.3.2. Case 2: Eccentric, Longer Period

Table 1 and 3 summarises the model and orbit fitting results for the second test case. Additional, useful figures are included in Appendix C.2.

With the longer period orbit, a smaller arc has been sampled by the observing cadence. Naturally, this widens the posterior distribution on the orbital parameters and the relative errors of the MAP. Although across a 3 year period the trajectory exhibits less curvature than in Case 1, the narrow 1σ error bars still result in a confident detection of a curved trajectory, with the FAR near 0. Despite the total flux density being at the edge of BHEX binary detectability, the sensitivity provided by observations with the ground using FPT, and the contributions of multiple, independent baselines results in a very accurate estimation of the source positions.

a and e are still very well constrained. Despite $< \frac{1}{3} P_{\text{obs}}$ having been sampled, a strong preference for an eccentricity ~ 0.5 can be seen. Mass ratio q is essentially unconstrained by the data and this is evident throughout the test cases. As with Case 1, the posterior distribution of i suggests a low inclination but it is very wide. This is further evidence of the difficulty in estimating incli-

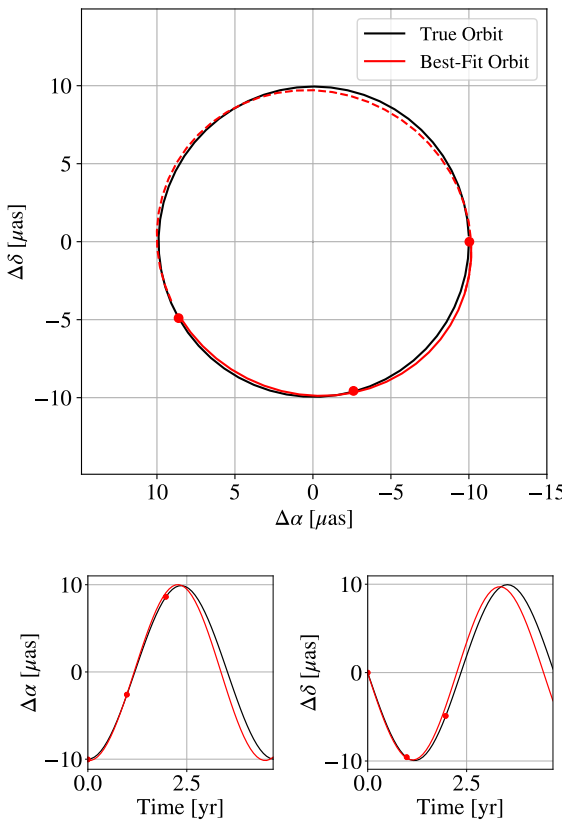


Fig. 5. (Top) Best-fit solution for Case 1. Observed positions of secondary relative to the primary are indicated by red markers with 1σ error bars. (Bottom) Relative right ascension and declination.

Table 2. Case 1 orbit fitting posterior distribution summary. Error between fitted value and true parameter value given in brackets for MAP. Median provided with 68% credible interval ranges.

Parameter	True	MAP	Median
$M [10^9 M_\odot]$	0.400	0.483 (20.9%)	$0.492^{+0.031}_{-0.022}$
$q [-]$	1.000	0.293 (70.7%)	$0.554^{+0.307}_{-0.347}$
$a [\text{pc}]$	0.0101	0.0104 (2.67%)	$0.0106^{+0.00082}_{-0.00025}$
$e [-]$	0.000	0.00844	$0.0368^{+0.115}_{-0.024}$
$i [^\circ]$	0	18.39	$24.8^{+6.9}_{-5.3}$
$\omega [^\circ]$	0	54.35	$185.8^{+95.5}_{-169.3}$
$\Omega [^\circ]$	0	208.7	$67.3^{+150.0}_{-42.8}$
$\tau [-]$	0	0.737	$0.148^{+0.668}_{-0.074}$

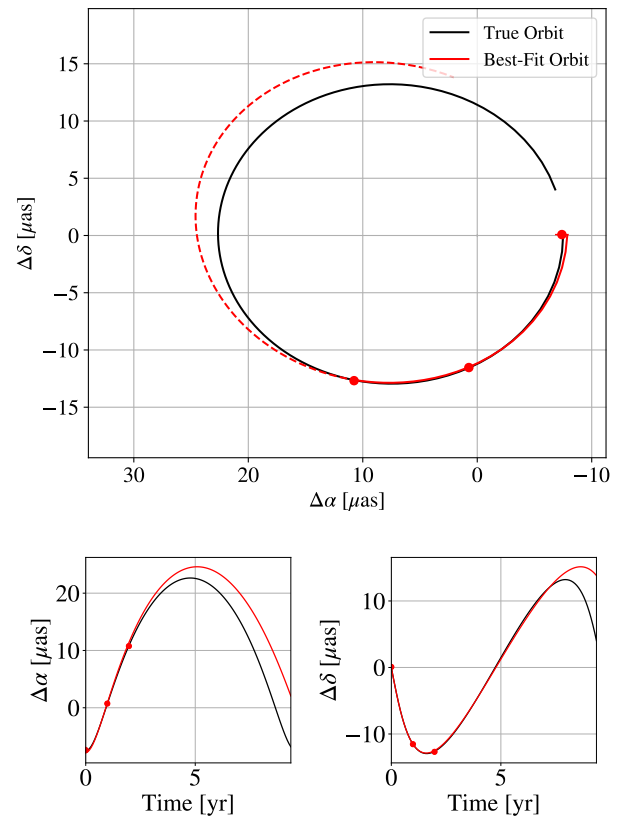


Fig. 6. (Top) Best-fit solution for Case 2. Observed positions of secondary relative to the primary are indicated by red markers with 1σ error bars. (Bottom) Relative right ascension and declination.

Table 3. Case 2 orbit fitting posterior distribution summary. Error between fitted value and true parameter value given in brackets for MAP. Median provided with 68% credible interval ranges.

Parameter	True	MAP	Median
$M [10^9 M_\odot]$	0.337	0.346 (2.6%)	$0.370^{+0.122}_{-0.022}$
$q [-]$	1.000	0.548 (45.2%)	$0.669^{+0.277}_{-0.445}$
$a [\text{pc}]$	0.0152	0.0164 (7.96%)	$0.0169^{+0.0091}_{-0.0010}$
$e [-]$	0.500	0.516 (3.13%)	$0.525^{+0.149}_{-0.027}$
$i [^\circ]$	0	2.75	$10.46^{+30.7}_{-6.39}$
$\omega [^\circ]$	0	190.9	$145.8^{+139.4}_{-120.6}$
$\Omega [^\circ]$	0	175.8	$233.8^{+110.2}_{-144.4}$
$\tau [-]$	0	0.00486	$0.00676^{+0.00336}_{-0.00254}$

nation without prior constraints. Interestingly, the MAP solution has a very low inclination. In Ω and ω (the true values of which are both 0°), multiple effects can be seen: the diagonal ridge in the Ω vs. ω plot shows multimodality as many combinations of angular parameters can result in similar projected tracks on the sky; wrap-around as expected for parameters ranging from 0 – 360° ; an expected 180° degeneracy between the parameters (see the MAP solution where both parameters are $\sim 180^\circ$ offset from the truth). τ is showing a very strong preference for 0 with some wrap-around to 1 as for an eccentric orbit, the periastron posi-

tion is more definitely defined than for the circular orbit in the previous case.

The posterior indicates a strong eccentric mode with low inclination and a well constrained total mass. The expected parameter degeneracies without more stringent prior constraints are also evident.

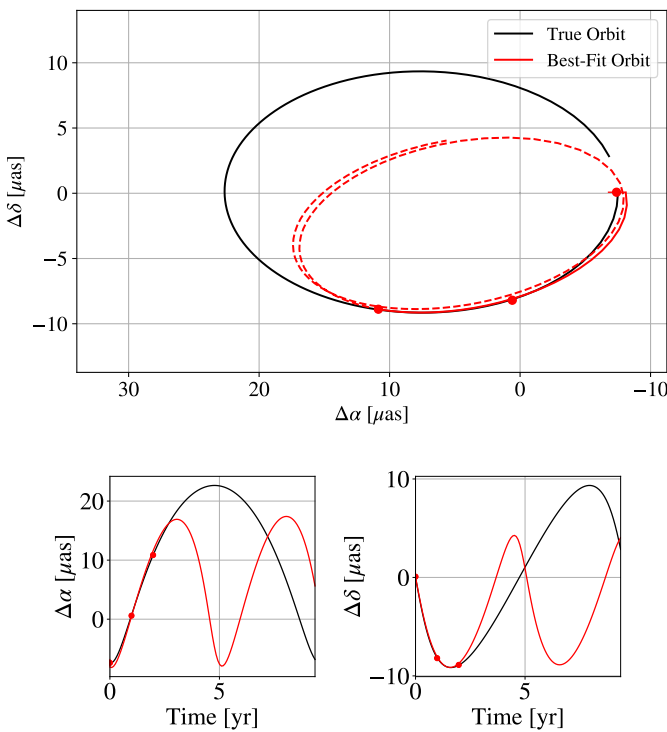


Fig. 7. (Top) Best-fit solution for Case 3. Observed positions of secondary relative to the primary are indicated by red markers with 1σ error bars. (Bottom) Relative right ascension and declination.

3.3.3. Case 3: Eccentric, Inclined

Table 1 and 4 summarises the model and orbit fitting results for the third test case. Additional, useful figures are included in Appendix C.2.

Although similar trends can be seen as in Case 2, the introduction of inclination appears to have reduced the multimodality, particularly in Ω and ω . a and e are fairly constrained but now the posterior is clearly wider and the MAP solution is further deviated from the truth. The posterior in M is also wider and q still shows that it is unconstrained. i is showing a clear tendency to a moderate inclination but the posterior is very wide. The most striking difference is in Ω and ω where there now appears to be a single, strong mode, suggesting the degeneracy is largely broken now the orbit is not face-on. A non-zero inclination breaks the commutativity of the rotations that define the projected angle of the orbit on the sky. However, the 180° degeneracy is still very clearly evident and this is also expected. As with Case 2, a very strong preference for $\tau = 0/1$ is illustrated. In the MAP solution, the effect of periastron precession is also evident supporting the need for a PN propagation in the orbit fitting methodology.

Case 3 shows the effect of sampling a short arc of the orbit as beyond the three observations, the best fit orbit deviates significantly from the truth and this appears to have been exaggerated through the introduction of inclination. Additional observations would evidently help with this issue, further constraining the right ascension and declination curves in the bottom of Fig. 7.

3.4. Identifying Candidates

Near-future capabilities will further progress the ability to identify and observe candidate binary systems. Through detection of Quasi-Periodic Oscillation (QPO) sources, the *Vera C. Rubin*

Table 4. Case 3 orbit fitting posterior distribution summary. Error between fitted value and true parameter value given in brackets for MAP. Median provided with 68% credible interval ranges.

Parameter	True	MAP	Median
$M [10^9 M_\odot]$	0.337	0.809 (139.9%)	$0.700^{+0.216}_{-0.276}$
$q [-]$	1.000	0.407 (59.3%)	$0.350^{+0.309}_{-0.144}$
$a [\text{pc}]$	0.0152	0.0133 (12.3%)	$0.0142^{+0.0036}_{-0.0012}$
$e [-]$	0.500	0.449 (10.2%)	$0.483^{+0.085}_{-0.056}$
$i [^\circ]$	45.0	58.7 (30.4%)	$55.8^{+4.0}_{-7.6}$
$\omega [^\circ]$	0	139.9	$147.1^{+34.5}_{-13.5}$
$\Omega [^\circ]$	0	173.5	$177.9^{+5.7}_{-7.7}$
$\tau [-]$	0	0.946	$0.957^{+0.035}_{-0.941}$

observatory may be able to detect hundreds to thousands of candidate SMBHBs, although with a preference for systems with short orbital periods such that statistically significant variability can be observed across the 10 year survey (Liao et al. 2020). Although certainty of a black hole binary will not be achieved with these observations, identification of likely candidates, with follow up radio observations, may provide sufficient evidence to warrant a VLBI observation. The detection of astrometric oscillations with VLBI proposed by Gurvits et al. (2025) also has potential for identification of more binary systems.

Agarwal et al. (2025) present a search for GW sources from 114 AGN, using the NANOGrav 15 yr dataset, by fixing priors for period and position on the sky from QPO data and fitting the PTA measurements for the remaining binary parameters. Bayesian model comparison with uncorrelated red noise identifies eight candidates with Bayes factors (BF) > 1 , albeit not with huge statistical significance. The sources: SDSS J153636.22+044127.0 ("Rohan") and SDSS J072908.71+400836.6 ("Gondor"), have BFs of 3.37(5) and 2.44(3) respectively. The predicted separations from QPO measurements are tantalisingly within BHEX's capabilities: 3.2 μ as and 15 μ as, respectively. Despite the lack of statistical significance, the method by which these candidates were identified is very promising and should result in more identifications, and with greater confidence in the future, as pulsar timing improves (Agarwal et al. 2025).

Using RadioAstron 22 GHz observations of the famed binary candidate OJ287 at 12 μ as, Valtonen et al. (2025) demonstrate that the 136 yr optical light curves and 40 yr radio jet observations can be explained with the presence of a secondary jet. OJ287 is a target source of BHEX and the improvement in resolution by a factor of 2 will enable further constraining of the possible explanations for its flaring behaviour. If a secondary jet can be confidently identified, the positions of the black holes at their bases could be estimated and the method presented in this paper used to fit an orbit.

The Event Horizon and Environs (ETHER) database, used for identification of EHT and ngEHT targets, is also building a library of SMBHB candidates identified using the methods described previously (Ramakrishnan et al. 2023). With follow-up observations of promising candidates with VLBI planned to constrain flux densities and determine detectability, the ETHER

database will no doubt play an important role in identifying binary targets.

4. Discussion

The binary parameter space detectable by BHEX has been constrained, with the sources requiring $F_{v,\text{tot}} \geq 0.04$ Jy, if realistic thermal noise values are assumed across the array. Assuming that the flux density is distributed between the two black hole components proportional to their mass, binary detectability with BHEX favours near-equal mass systems with $q \geq 0.75$ at the minimum detectable flux density. If the secondary source is more active than the primary (as predicted in GRMHD), or the total flux of the source approaches 0.5 Jy, the observable mass ratio could be greatly reduced to $q \sim 0.01$. Binaries are detectable (under the conditions described in Section 3.1) even for separations down to 2 μ as, although these would be unresolved. BHEX is an extension to a ground-based array, with overlap with the ngEHT. As such, apart from the minimum separation, the above constraints will also broadly apply to the ngEHT.

As shown in Fig. 1, with the contributions of multiple independent baseline measurements of the source, the achievable astrometric precision is very low resulting in confident detection of non-linear motion for long period orbits. If the binary has period $P_{\text{obs}} \leq 23$ years, a curved trajectory can be confidently detected for a source with $F_{v,\text{tot}} = 0.05$ Jy and separation 6 μ as, with only 3 annual observations. This maximum period increases with increasing angular separation.

Across the three primary test cases, clear trends in the orbit fitting can be seen. Semi-major axis (a) and eccentricity (e) are constrained to within 13% of the true values, for all cases. Total mass M also demonstrates a tight posterior distribution, and this could be further constrained if more stringent prior constraints from observational evidence are included. Inclination is more difficult to constrain as various combinations of a, e and i can produce similar projected trajectories on the sky. Ω and ω show the expected 180° reflection degeneracy in all cases, but much of the additional multimodality is broken for inclined orbits. Mass ratio q is essentially unconstrained across all cases as, considering the Keplerian equation for orbital period, $P_{\text{obs}} \propto \frac{a^3}{M}$, it is only dependent on total mass and semi-major axis. The small number of observations that are likely to be possible with BHEX does present issues in tightly constraining orbits for which only a short arc is sampled. Naturally, more observations will always result in better fits of such cases.

The supplementary test cases support the trends described above whilst illustrating the effect of additional parameter variations. In Case 5, the effect of a more diffuse source on the astrometric uncertainty is demonstrated. $\sigma_{\text{pos,av}}$ rises from $\sim 0.1^\circ$ to 0.64° in this case, as the source has lower brightness and is less compact. The effect of this can then be seen in the wider posterior distribution and increased relative errors in the MAP solution, compared to Case 4 for which a similar percentage of the orbit period has been sampled. In Case 6, an extreme inclination example results in the least well constrained orbit and a FAR of 100%, indicating that linear relative motion fits the data as well as or better than the orbital solution. This is because the three observations show very little variation in declination as the binary is almost edge on. This case also depicts the increased astrometric uncertainty for sources with separation below BHEX resolution, as can be seen for the first observed position. In Case 7, a longer period case is considered of 30 years. Here a very small arc of the orbit is sampled by three BHEX observations

and this is reflected in the FAR which is also 100%. This supports the predictions made with the analytic estimate of the minimum number of observations required to reject linear motion in Fig. 1.

The primary contribution of BHEX is finer angular resolution. As such, the example cases shown here with angular separations $\gtrsim 15 \mu$ as would also be detectable from the ground (e.g., ngEHT). The constraint on total number of observations disappears with ground observations and the effect of increased sampling of the orbit period can clearly be seen in the goodness of fit of the orbits for Case 1 and Case 4. The challenge, as discussed in Section 3.4, is finding candidate sources.

If BHEX could successfully detect a binary source, and observe orbital motion over the course of the mission, this would be the first direct evidence of the existence of sub-parsec SMBHBs, supporting existing evidence from GW detections. Although this in itself would be a major achievement, the real scientific value would be to do this for a statistically significant population of binaries. As described by D’Orazio & Loeb (2018), a sample of massive binary separations and their redshift distribution would enable models for residence times to be ruled out and the parameters defining these models to be constrained. Such observations would also be beneficial in calibrating existing methods for binary candidate identification that are perhaps easier to perform than spaceborne VLBI. Such a survey would require a future spaceborne VLBI system, with a longer mission lifetime than BHEX and more specifically designed for SMBHB observation. This is discussed further in Section 4.2.

Any observing time with BHEX dedicated to binary candidates is going to be inherently limited by the short lifetime and the primary science objectives of the mission. In this case, if sufficient observations of a candidate cannot be performed to confirm orbital motion, BHEX measurements could form part of a longer term, multi-instrument system observing the same source. This could consist of the ngEHT and/or future spaceborne VLBI systems.

4.1. Image Reconstruction

Reconstructed images from the VLBI data are the ultimate goal in the effort to directly observe a supermassive black hole binary. Generating images has multiple benefits compared to working directly with the correlated visibility data. The toy model used here is a simple depiction of a binary appearance, consisting of only two Gaussian sources. In reality, the binary is likely to consist of a combination of Gaussian-like emission, jet launching and other emission regions due to the interaction of the accretion flow between two close SMBHBs. Reconstructing an image removes some of this complication, allowing the various emission regions to be more intuitively analysed. Also, where the (u, v) coverage is sparse, imaging algorithms incorporate prior information to fill missing Fourier components, aiming to give a more faithful representation of the source structure. Chael et al. (2018) provide a review of VLBI image reconstruction and present the methodology used in the `eht-imaging` package.

High fidelity image reconstruction requires as dense (u, v) coverage as possible. Images of new black hole shadows, jets and the photon rings of M87* and Sgr A* are intended to be reconstructed using BHEX data. With an extensive ground array, BHEX will therefore achieve sufficient (u, v) coverage for image reconstruction of complex sources. In this work we have shown that BHEX is capable of confidently distinguishing a binary Gaussian model from a single Gaussian. A future space-

bore VLBI mission, capable of studying SMBHBs must be designed with the need for very dense (u, v) coverage in mind.

4.2. Requirements for Future Spaceborne VLBI

The angular resolution and sensitivity of BHEX have been primarily driven by the photon ring science. Furthermore, as shown by Fig. 2, BHEX's performance is predicted to only enable observation of a few tens of binary systems, with significant uncertainty existing in this model. To observe a statistically significant number of binary systems, enough to constrain evolutionary models and draw conclusions about the distribution of binaries across redshift and in relation to their host galaxy, a more performant interferometer is required.

As shown in Fig. 2, to significantly increase the number of observable systems, angular resolution and sensitivity ideally need to be improved by an order of magnitude compared to BHEX. We set the angular resolution requirement to that originally defined for the THEZA concept, $1 \mu\text{as}$. Furthermore, as shown by the results of D'Orazio & Loeb (2018), the number of observable systems becomes sensitivity-limited beyond this point, with minimal increase with further improving resolution.

As described above, dense (u, v) coverage is required for image reconstruction, with sampling of the Fourier domain of the source across a range of baseline lengths and orientations preferable. For a spaceborne system in orbit around the Earth and observing with a ground array, this is at odds with the need for fine angular resolution. The latter requires extreme distance from the Earth (with observing frequency limited by the ground array) whilst the former is more easily achieved with rapid orbital motion associated with short orbital periods at lower altitudes. To achieve both of these effects, multiple space elements are required. A proposed orbit for a dual-element THEZA system in orbit around the Earth is shown by Hudson et al. (2023) which provides the desired (u, v) coverage features.

Scheduling observations with an extensive ground array poses considerable difficulty and limits the available observing time for a spaceborne VLBI mission. The observing frequency of the array is also effectively limited by atmospheric absorption. It is therefore desirable to have a multi-element spaceborne VLBI system, capable of observing independently from the ground to overcome these issues. As such, a minimum of three elements would enable closure phases to be measured around the triangle of antennae which provides considerable benefits for calibration and imaging (Chael et al. 2018). Observations with a ground array should also be possible for extremely dense (u, v) coverage and to make use of the low SEFD sites on the ground. Therefore a minimum dual-band system is required to fully exploit both scenarios.

Considering the data handling issues associated with spaceborne VLBI (see extensive discussion on this for BHEX by Hudson et al. (2025)), operation as close to the Earth as possible is beneficial for achieving high data rates for downlinking to the ground. The need for high orbit determination accuracy of the spacecraft is also more easily achieved close to the Earth. Combining this with the practical limitation of launch costs makes an Earth orbiting system most realistic. The short mission lifetime of BHEX is also not conducive to detecting orbital motion in longer period binaries. The proposed capabilities and features of a THEZA-like spaceborne VLBI concept for observing a statistically significant population of binaries (as well as performing many other transformative radio studies) are provided in Table 5.

Table 5. THEZA mission preliminary capabilities definition.

Parameter	Value
Angular Resolution (θ_r)	$1 \mu\text{as}$
Baseline Sensitivity (S_v)	$< 1 \text{ mJy}$
Observing Frequencies	$\sim 320 \text{ & } \geq 590 \text{ GHz}$
No. of spaceborne elements	≥ 3
Mission Lifetime	$> 5 \text{ years}$
Orbit Regime	Earth Orbit

Such a mission would be of a different class to BHEX, requiring a significantly higher budget and additional technological advances. Gurvits et al. (2022) discuss the key engineering challenges that must be tackled to realise future spaceborne VLBI missions.

5. Conclusions

Conclusive electromagnetic evidence of a sub-parsec, supermassive black hole binary (SMBHB) would be a major achievement given its relevance to some of the most important, ongoing research in astrophysics. Very Long Baseline Interferometry (VLBI) is the only astronomical technique with the resolution and sensitivity to directly observe such a system and spaceborne VLBI is required to observe a statistically significant population. The black Hole Explorer (BHEX) is the most likely mission to be realised in the near-future and we have shown that, although on the edge of its proposed capability, it would be theoretically capable of providing the first detection of an SMBHB.

Confirming that an observed source is indeed a binary is a challenge and observational signatures have been discussed that could be used to build confidence in a detection. Observing orbital motion with observations over multiple epochs would be the key evidence although BHEX is not best suited to this activity given its short, nominally 2 year, mission lifetime. However, the fine resolution and extensive (u, v) coverage provided by BHEX would be highly beneficial in resolving finer structure in the source and perhaps enabling observation of systems that would not be possible with just the ground array. The next steps to further the case for performing binary observations with BHEX requires that candidate sources are identified in time for launch. Promising methods to do this have also been reviewed.

Although BHEX will be a transformational interferometer, to perform a survey of a statistically significant sample of SMBHBs requires a more performant system. Estimating orbital parameters of a larger number of SMBHBs is necessary for constraining evolutionary models and drawing conclusions about their relationship with the host galaxy. Preliminary requirements of such a system have been defined as a first step towards realising a mission capable of reconstructing images of a sample of binaries. The orbit fitting methodology presented here and used throughout the paper can serve as a building block of an analysis pipeline for processing VLBI data of SMBHB candidates in the future.

Acknowledgements. The authors would like to acknowledge the use of the Delft-Blue computing cluster, managed by TU Delft, which was essential for running the computationally expensive examples presented in this paper (Delft High Performance Computing Centre DHPC). We also wish to acknowledge the entirety of the BHEX community for their ongoing efforts to realise this exciting mission. Finally, the lead author would like to thank his employer, KISPE, for providing him with the flexibility and support to study for a PhD alongside his full-time role.

References

Agarwal, N., Agazie, G., Anumarlapudi, A., et al. 2025, The NANOGrav 15 yr Data Set: Targeted Searches for Supermassive Black Hole Binaries, arXiv:2508.16534 [astro-ph]

Agazie, G., Anumarlapudi, A., Archibald, A. M., et al. 2023, The Astrophysical Journal Letters, 951, L8, publisher: American Astronomical Society

Ayzenberg, D., Blackburn, L., Brito, R., et al. 2025, Living Reviews in Relativity, 28, publisher: Springer Science and Business Media LLC

Bardeen, J. M. 1973, Timelike and null geodesics in the Kerr metric., aDS Bibcode: 1973blho.conf..215B

Begelman, M. C., Blandford, R. D., & Rees, M. J. 1980, Nature, 287, 307

Blanchet, L. 2024, Living Reviews in Relativity, 27, 4

Blunt, S., Nielsen, E. L., De Rosa, R. J., et al. 2017, The Astronomical Journal, 153, 229, publisher: American Astronomical Society

Callegari, S., Kazantzidis, S., Mayer, L., et al. 2011, The Astrophysical Journal, 729, 85

Chael, A., Lupsasca, A., Wong, G. N., & Quataert, E. 2023, ApJ, 958, 65

Chael, A. A., Johnson, M. D., Bouman, K. L., et al. 2018, The Astrophysical Journal, 857, 23

Colpi, M., Danzmann, K., Hewitson, M., et al. 2024, arXiv e-prints, arXiv:2402.07571, LISA Definition Study Report, ESA-SCI-DIR-RP-002

Delft High Performance Computing Centre (DHPC). 2024, DelftBlue Supercomputer (Phase 2), <https://www.tudelft.nl/dhpc/ark:/44463/DelftBluePhase2>

Dey, L., Valtonen, M. J., Gopakumar, A., et al. 2018, The Astrophysical Journal, 866, 11

Doeleman, S. S., Barrett, J., Blackburn, L., et al. 2023, Galaxies, 11, 107

D’Orazio, D. J., Charisi, M., Derdzinski, A., et al. 2024, in Black Holes in the Era of Gravitational-Wave Astronomy, ed. M. Arcà Sedda, E. Bortolas, & M. Spera (Elsevier), 379–478, (updated version: arXiv:2310.16896)

D’Orazio, D. J., Haiman, Z., Duffell, P., MacFadyen, A., & Farris, B. 2016, Monthly Notices of the Royal Astronomical Society, 459, 2379

D’Orazio, D. J., Haiman, Z., & MacFadyen, A. 2013, Monthly Notices of the Royal Astronomical Society, 436, 2997

D’Orazio, D. J., Haiman, Z., & Schiminovich, D. 2015, Nature, 525, 351

Dosopoulou, F. & Antonini, F. 2017, The Astrophysical Journal, 840, 31

D’Orazio, D. J. & Loeb, A. 2018, The Astrophysical Journal, 863, 185, publisher: American Astronomical Society

Event Horizon Telescope Collaboration, Akiyama, K., Alberdi, A., et al. 2022, The Astrophysical Journal Letters, 930, L12, publisher: American Astronomical Society

Event Horizon Telescope Collaboration, Akiyama, K., Alberdi, A., et al. 2019, The Astrophysical Journal Letters, 875, L1, publisher: American Astronomical Society

Fang, Y. & Yang, H. 2022, The Astrophysical Journal, 927, 93

Farris, B. D., Duffell, P., MacFadyen, A. I., & Haiman, Z. 2014, The Astrophysical Journal, 783, 134

Gergely, L. A. & Biermann, P. L. 2009, The Astrophysical Journal, 697, 1621

Gualandris, A., Read, J. I., Dehnen, W., & Bortolas, E. 2017, Monthly Notices of the Royal Astronomical Society, 464, 2301

Gurvits, L. I., Paragi, Z., Amils, R. I., et al. 2022, Acta Astronautica, 196, 314, publisher: Elsevier BV

Gurvits, L. I., Paragi, Z., Casasola, V., et al. 2021, Experimental Astronomy, 51, 559, publisher: Springer Science and Business Media LLC

Gurvits, L. I., Polnarev, A. G., Frey, S., et al. 2025, A&A, 700, A168

Hou, Y., Huang, J., Guo, M., Mizuno, Y., & Chen, B. 2025, The Astrophysical Journal, 988, L51, publisher: IOP ADS Bibcode: 2025ApJ...988L..51H

Hudson, B., Gurvits, L. I., Palumbo, D., Issaoun, S., & Rana, H. 2025, Acta Astronautica, 232, 564

Hudson, B., Gurvits, L. I., Wielgus, M., et al. 2023, Acta Astronautica, 213, 681, publisher: Elsevier BV

Issaoun, S., Pesce, D. W., Rioja, M. J., et al. 2025, The Astronomical Journal, 169, 229, publisher: IOP ADS Bibcode: 2025AJ....169..229I

Johnson, M., Akiyama, K., Baturin, R., et al. 2024, in Space Telescopes and Instrumentation 2024: Optical, Infrared, and Millimeter Wave, ed. L. E. Coyle, M. D. Perrin, & S. Matsuura (Yokohama, Japan: SPIE), 90

Kormendy, J. & Ho, L. C. 2013, Annual Review of Astronomy and Astrophysics, 51, 511

Liao, W.-T., Chen, Y.-C., Liu, X., et al. 2020, Monthly Notices of the Royal Astronomical Society, publisher: Oxford University Press (OUP)

Mayer, L. 2013, Classical and Quantum Gravity, 30, 244008

Merritt, D. & Milosavljević, M. 2005, Living Reviews in Relativity, 8, publisher: Springer Science and Business Media LLC

Palumbo, D. C. M. 2025, The Astrophysical Journal Letters, 978, L4

Palumbo, D. C. M., Wong, G. N., & Prather, B. S. 2020, The Astrophysical Journal, 894, 156

Pati, M. E. & Will, C. M. 2002, Physical Review D, 65, publisher: American Physical Society (APS)

Pearce, L. A., Kraus, A. L., Dupuy, T. J., et al. 2020, The Astrophysical Journal, 894, 115, publisher: American Astronomical Society

Pesce, D. W., Blackburn, L., Chaves, R., et al. 2024, The Astrophysical Journal, 968, 69

Pesce, D. W., Palumbo, D. C. M., Narayan, R., et al. 2021, The Astrophysical Journal, 923, 260, publisher: American Astronomical Society

Piarulli, M., Marsat, S., Sänger, E. M., et al. 2025, arXiv e-prints, arXiv:2510.06330

Ramakrishnan, V., Nagar, N., Arratia, V., et al. 2023, Galaxies, 11, 15

Ricarte, A., Natarajan, P., Narayan, R., & Palumbo, D. C. M. 2025, ApJ, 980, 136

Ricarte, A., Tiede, P., Emami, R., Tamar, A., & Natarajan, P. 2023, Galaxies, 11, 6

Rioja, M., Dodson, R., Malarecki, J., & Asaki, Y. 2011, The Astronomical Journal, 142, 157, publisher: American Astronomical Society

Rioja, M. J. & Dodson, R. 2020, The Astronomy and Astrophysics Review, 28, publisher: Springer Science and Business Media LLC

Ruffa, I., Davis, T. A., Elford, J. S., et al. 2023, Monthly Notices of the Royal Astronomical Society: Letters, 528, L76

Sala, L., Valentini, M., Biffi, V., & Dolag, K. 2024, A&A, 685, A92

Sayeb, M., Blecha, L., Kelley, L. Z., et al. 2021, Monthly Notices of the Royal Astronomical Society, 501, 2531

Speagle, J. S. 2020, Monthly Notices of the Royal Astronomical Society, 493, 3132, publisher: OUP ADS Bibcode: 2020MNRAS.493.3132S

Tang, Y., MacFadyen, A., & Haiman, Z. 2017, Monthly Notices of the Royal Astronomical Society, 469, 4258

Thompson, W., Lawrence, J., Blakely, D., et al. 2023, The Astronomical Journal, 166, 164

Valtonen, M. J., Dey, L., Zola, S., et al. 2025, Identifying the secondary jet in the RadioAstron image of OJ~287, arXiv:2510.06744 [astro-ph]

Wong, G. N., Chael, A., Lupsasca, A., & Quataert, E. 2025, Black Hole Polarimetry II: The Connection Between Spin and Polarization, aDS Bibcode: 2025arXiv250922639W

Zhao, S.-S., Jiang, W., Lu, R.-S., Huang, L., & Shen, Z. 2024, The Astrophysical Journal, 961, 20

Appendix A: Orbit Model Error Analysis

The PN orbit propagation used to evaluate the likelihood of candidates in the orbit fitting method has been implemented up to order 3.5PN. Provided in this section is an evaluation of the order of magnitude impact of higher orders and other relativistic effects on the observed black hole positions.

The terms up to 3PN produce the characteristic precession of an eccentric orbit that occurs on the order of single orbital periods. This behaviour is desired in this model as the precessing nature of the orbit considerably changes the observed position within the timescales of possible VLBI observations. The candidate SMBHB OJ287 exhibits $\sim 40^\circ$ per ~ 12 year orbit.

Each PN term has an associated expansion factor $(\frac{v}{c})^{2PN}$ where v is the orbital velocity vector. The PN terms therefore have the greatest effect when v is a maximum. Consider an orbit with $v = 0.1c$, over an orbital period of 20 years. Approximating the differential displacement due to 4PN acceleration term as $\Delta x \sim \frac{1}{2} \Delta a_N t^2$ where a_N is the Newtonian acceleration given by $\frac{GM}{r^2}$, a source at redshift 0.2 will only exhibit an angular displacement of 10^{-6} μas , far below resolution limits of VLBI.

The spin-orbit coupling effect produces a precession of the orbital plane which can be calculated from the equation provided by Dey et al. (2018). Considering the same example orbit as above, and black hole spins of $\chi_1 = \chi_2 = 0.5$, the precession rate after a single orbital period equates to a differential angular displacement of ~ 0.015 μas . The spin-spin coupling effect causes a precession of a lower order that results in an angular displacement of $\sim 10^{-4}$ μas .

For an inclined binary orbit, the relative time for light to travel from each source to the observer results in the farther black hole appearing in a position from an earlier time than the closer one. Considering the orbit above with a worst-case inclination of 90° , this effect causes the secondary black hole to appear at a position ~ 0.6 μas different to its real location at the time of the primary black hole's emission. At a tenth of the observed separation, this is by far the largest effect compared to higher orders of the PN propagation. With BHEX achieving astrometric uncertainties of ~ 0.1 μas , this is non-negligible. Table A.1 summarises these results.

To include the relative light travel time effect, the emission time (t_{emit}) of a black hole (i) observed at time t_{obs} in the binary rest frame is calculated from

$$t_{\text{emit},i} = t_{\text{obs},i} - \frac{1+z}{c} D_{\text{los}}(t_{\text{emit},i}) \quad (\text{A.1})$$

$D_{\text{los}}(t_{\text{emit},i}) = \mathbf{x}_i(t_{\text{emit},i}) \cdot \hat{\mathbf{n}}$ is the distance along the observer line of sight of the black hole from the binary barycentre. $\hat{\mathbf{n}}$ is the observer unit vector direction, which in this case is the z-axis. This is solved iteratively using a simple numerical method

$$t_{\text{emit},i}^{n+1} = t_{\text{obs},i} - \frac{1+z}{c} D_{\text{los}}(t_{\text{emit},i}^n) \quad (\text{A.2})$$

The observed position of each black hole is then $\mathbf{x}_i^{\text{obs}}(t_{\text{obs}}) = \mathbf{x}_i(t_{\text{emit},i})$. The coordinate system is transformed to place the primary black hole at the origin and the relative right ascension and declination of the secondary are computed by projecting the observed position in the binary rest frame onto the sky plane and converting to angular units. This approach also includes the time dilation effect of the source being at redshift z on the relative light travel time.

Table A.1. Orbit model error analysis of higher order PN terms and relativistic effects. Differential angular displacements provided for an example orbit with $P_{\text{obs}} = 20$ years, $\theta_r = 6 \mu\text{as}$, $v = 0.1c$.

Effect	$\sim \Delta\theta [\mu\text{as}]$
Relative light travel time	0.6
Spin-orbit coupling	0.015
Spin-spin coupling	10^{-4}
$\geq 4\text{PN}$ terms	10^{-6}

Appendix B: Minimum Number of Observations

In this section is provided the full derivation of Eq. 4. For a face-on, circular orbit, the projected motion on the sky in right ascension α is

$$\alpha = a \cos\left(\frac{2\pi t}{P_{\text{obs}}}\right)$$

where a is the orbit semi-major axis in μas . For small $t \ll P_{\text{obs}}$, we expand in a Taylor series

$$\alpha \approx a - \frac{1}{2} a \left(\frac{2\pi t}{P_{\text{obs}}}\right)^2 = a \left(1 - \frac{1}{2} \left(\frac{2\pi t}{P_{\text{obs}}}\right)^2\right)$$

Thus, the maximum deviation from linear motion over a time span T is approximately

$$\Delta\alpha_{\text{max}} \sim a \left(\frac{\pi T}{P_{\text{obs}}}\right)^2$$

Assuming N_{min} observations spaced by cadence τ , the total span is $T = (N_{\text{min}} - 1)t_{\text{cad}}$, so:

$$\Delta\alpha_{\text{max}} \sim a \left(\frac{\pi(N_{\text{min}} - 1)t_{\text{cad}}}{P_{\text{obs}}}\right)^2$$

To statistically detect this curvature, we require:

$$\Delta\alpha_{\text{max}} \gtrsim k\sigma_{\text{pos}}$$

for some significance threshold k (e.g., $k = 3$ or 5) and where σ_{pos} is the uncertainty in the position estimation of the secondary black hole. Substituting and solving for N_{min} , we get

$$a \left(\frac{\pi(N_{\text{min}} - 1)t_{\text{cad}}}{P_{\text{obs}}}\right)^2 \geq k\sigma_{\text{pos}}$$

$$N_{\text{min}} \geq 1 + \sqrt{\frac{k\sigma_{\text{pos}}^2 P_{\text{obs}}^2}{a\pi^2 t_{\text{cad}}^2}}$$

Since at least three observations are required to geometrically detect curvature, we enforce:

$$N_{\text{min}} = \max\left(3, \left\lceil 1 + \sqrt{\frac{k\sigma_{\text{pos}}^2 P_{\text{obs}}^2}{a\pi^2 t_{\text{cad}}^2 \cos i}} \right\rceil\right)$$

The effect of inclination can be introduced with the simple addition of a $\cos i$ term in the denominator as it reduces the projected separation by this factor.

The derivation of this equation approximates the curvature of a circular orbit using a Taylor expansion to the quadratic order. As such, its accuracy diminishes as the total elapsed time of observations approaches half of the orbital period of the binary. However, this will always underestimate the actual curvature of the orbit, still providing a conservative estimate of N_{min} .

Table C.1. BHEX VLBI observation properties.

Parameter	Value
Antenna Diameter	3.4 m
Surface Accuracy	40 μm
High-band LO Frequency	308 GHz
Low-band LO Frequency	86 GHz
Receiver Noise Temperature	40 K
Bandwidth	8 GHz
Pre-FPT Low-band t_{int}	45 s
Pre-FPT High-band t_{int}	10 s
Post-FPT High-band t_{int}	600 s
Quantisation	1 bit

Table C.2. Array properties. Median System Equivalent Flux Density (SEFD) ranges provided for high-band and low-band, accounting for variation across the three observing sessions. Where N/A is noted, this site could not observe in the defined band. For each site, it is defined whether it participates as part of the Northern (N) array or Southern (S) or both.

Site	Array	Diameter [m]	SEFD (High-band)	SEFD (Low-band)
ALMA	N & S	75	157 – 163	N/A
LMT	N & S	50	854 – 876	169 – 171
SMA	N & S	15	3313 – 3491	N/A
JCMT	N & S	15	3408 – 3591	1680 – 1688
IRAM	N	30	1955 – 2177	N/A
GLT	N	12	18824 – 20008	N/A
KP	N	12	N/A	3093 – 3197
GBT	N	100	N/A	204 – 208
BHEX	N & S	3.4	39817	19207

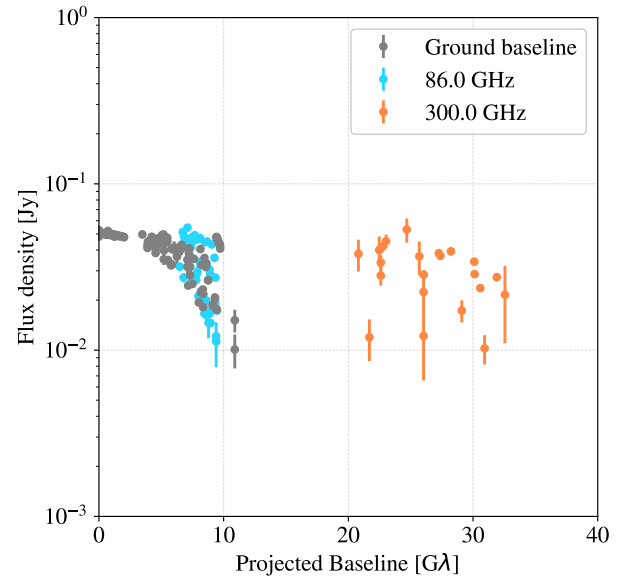
Appendix C: Simulated Observations

C.1. Simulation Configuration

Provided in this section are the definitions of key simulation properties used in the `ngehtsim` and `eht-imaging` simulations presented in Section 3.1. Table C.1 describes the modelled parameters for BHEX. Table C.2 defines the ground array used in the simulation. Provided for ALMA is an effective diameter that accounts for multiple antenna being phased together during observations.

Weather conditions at each ground site are also modelled, and an assumption of median weather conditions is used for these simulations. BHEX will utilise a northern ground array for January–March observations and a southern array for June–August. For all cases in Section 3.3, it is assumed the source lies close to M87* and therefore the January–March window is utilised, with ALMA participating in the observations but not performing FPT. We include a 10% error on complex visibilities as a proxy for typical errors that remain after gain calibration, and fit amplitudes and closure phases due to the absence of phase calibration in typical VLBI.

The reader is referred to Johnson et al. (2024) and the accompanying SPIE papers for more information on the design of BHEX and the full documentation of `eht-imaging` and `ngehtsim` for descriptions of how these simulations are performed.

**Fig. C.1.** BHEX and ground array detections of Case 1 binary source for first observation epoch.

C.2. Supplementary Simulation Material

Supplementary figures for Case 1, 2 and 3 are provided in this Section. Fig. C.1 depicts the simulated observational data for the first epoch of Case 1. Figures C.3 and C.4 show the toy models for Cases 2 and 3. Figures C.2, C.9 and C.10 show the posterior distribution of the runs in the form of corner plots.

Table C.3 summarises the additional observation and orbit fitting simulation results for BHEX. This provides a better understanding of the variation in the binary-observing performance of BHEX, across the parameter space. Justification for the choice of model parameters is provided below:

4. The estimated parameters of the source "Gondor" from Agarwal et al. (2025). Demonstration of observing a source with a wider separation at redshift $z = 0.07$. The source "Rohan" lies outside of the millimetre fundamental plane at $z = 0.38$ when the total flux density is set to the minimum detectable by BHEX (Ruffa et al. 2023). Therefore, if it exists, it is unlikely to be observable.
5. An extreme mass ratio example with total flux density similar to that of M87*, at the edge of BHEX binary detectability. Redshift $z = 0.05$ and black hole masses are calculated to meet prescribed period and separation.
6. An extreme inclination example such that the source is almost completely edge-on. Parameters the same as Case 3 in the main body of text but with an inclination of 80° . This case also demonstrates the scenario of the two sources having a separation smaller than BHEX resolution.
7. A long period example. In order to keep this case close to the fundamental millimetre plane, the separation is very wide (Ruffa et al. 2023). As such, if it existed, such a system would likely be observable from the ground. It is included here to demonstrate the effect of a long period orbit on the orbit fitting. Redshift $z = 0.05$.

Tables C.4, C.5, C.6 and C.7 present the orbit fitting results of the supplementary test cases and Fig. C.5, C.6, C.7 and C.8 depict the image models.

Table C.3. Supplementary test case summary. For all cases, Ω , ω and τ are set to 0 as they are expected to have less impact on the orbit fitting than the varied parameters. χ^2_{amp} and χ^2_{cp} describe the average goodness of fit of the binary Gaussian model in amplitude and closure phase to the observed data in eht-imaging, across the three observation epochs. The subscript *sin* describes the χ^2 values for fitting a single Gaussian source to the observed data. χ^2_{orb} describes the goodness of fit of the MAP orbital solution.

Case	$F_{\nu,\text{tot}}$ [Jy]	q	P_{obs} [yr]	Separation [μas]	e [-]	i [$^\circ$]	M [$10^8 M_\odot$]	$\text{FWHM}_{1/2}$ [μas]
4	0.03/0.02	0.6	4.41	15	0	0	56.2	2/1.6
5	0.47/0.03	0.06	5	10	0	0	3.37	5/0.3
6	0.03/0.02	1	10	$r_p = 7.5, r_a = 22.5$	0.5	80	3.37	2/2
7	0.03/0.02	1	30	30	0	0	3.00	2/2
	νL_ν [ergs^{-1}]	χ^2_{amp}	χ^2_{cp}	$\chi^2_{amp,\text{sin}}$	$\chi^2_{cp,\text{sin}}$	$\sigma_{\text{pos,av}}$ [μas]	χ^2_{orb}	FAR [%]
4	$1.4/0.94 \times 10^{42}$	0.33	0.29	16.3	19.1	0.057	7.50	0
5	$9.9/0.55 \times 10^{42}$	0.056	0.081	2.46	1.87	0.075	5.43	0
6	$5.54/3.68 \times 10^{41}$	0.15	0.32	3.03	0.38	0.64	6.20	100
7	$5.54/3.68 \times 10^{41}$	0.30	0.29	16.4	10.4	0.094	12.1	100

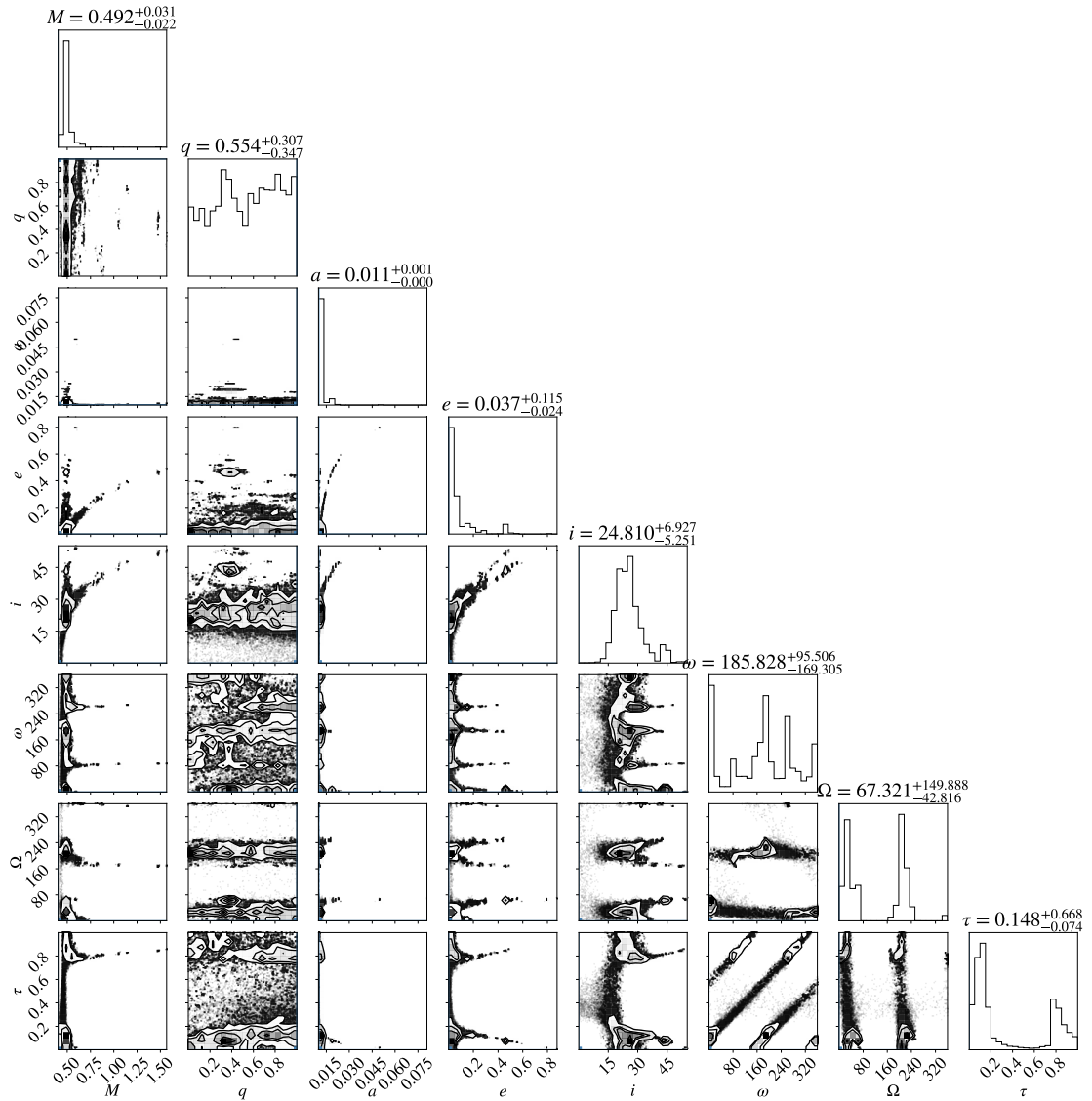
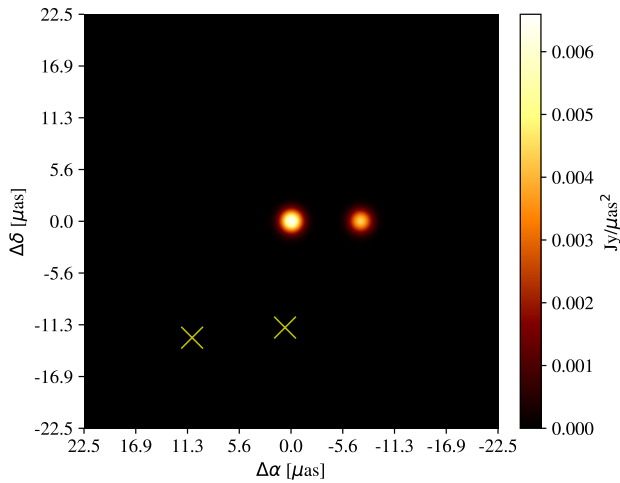
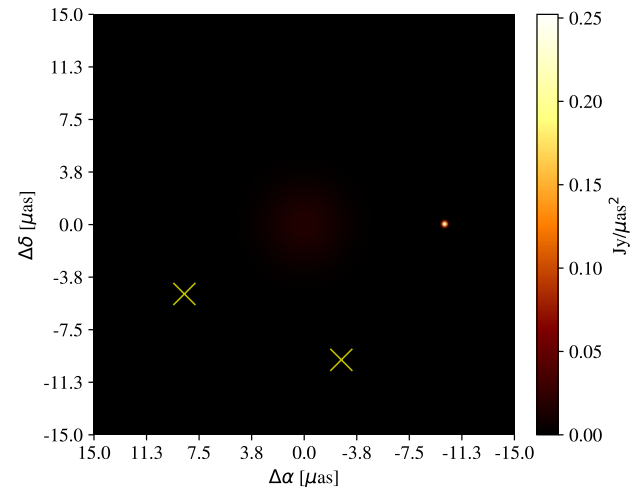
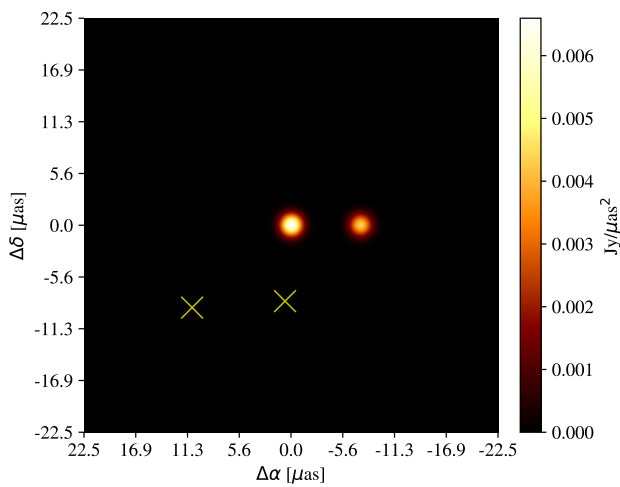
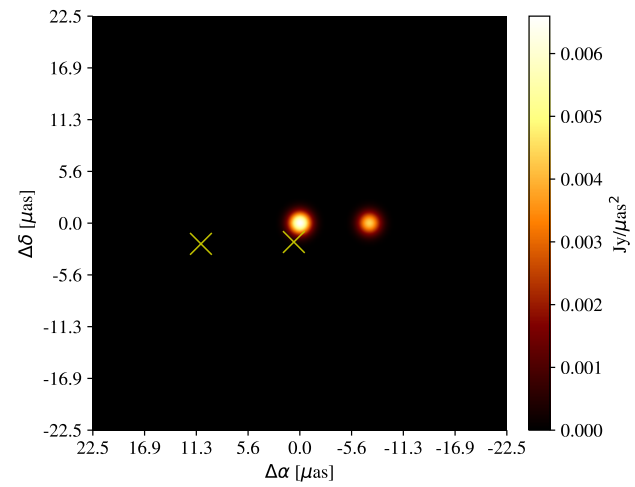
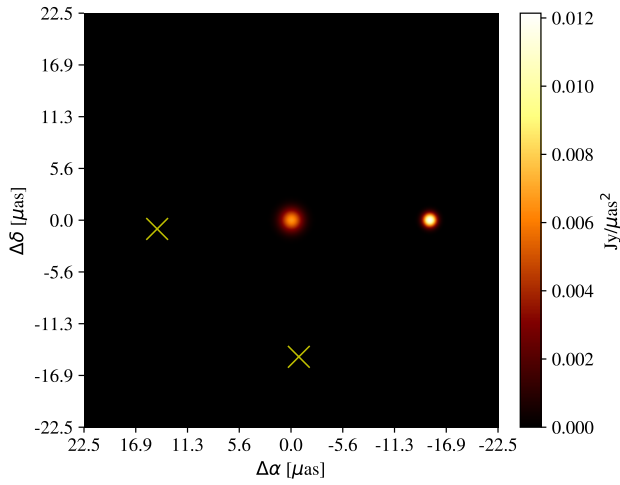
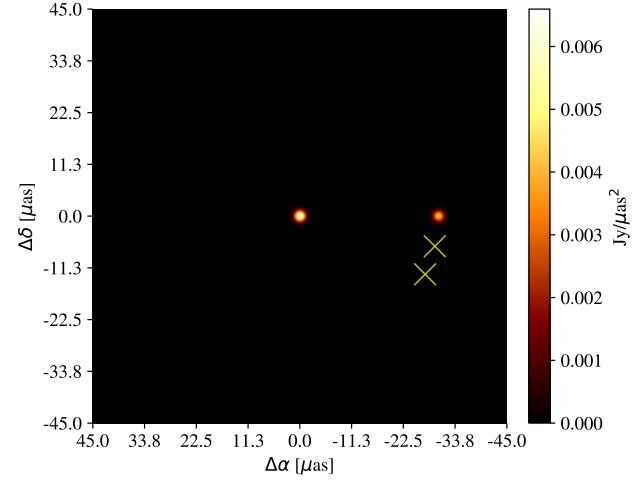


Fig. C.2. Case 1: Corner plot showing posterior distribution.

**Fig. C.3.** Stokes I image of the binary toy model for Case 2.**Fig. C.6.** Stokes I image of the binary toy model for Case 5. Primary source is very diffuse and therefore faint, located at the origin.**Fig. C.4.** Stokes I image of the binary toy model for Case 3.**Fig. C.7.** Stokes I image of the binary toy model for Case 6.**Fig. C.5.** Stokes I image of the binary toy model for Case 4.**Fig. C.8.** Stokes I image of the binary toy model for Case 7.

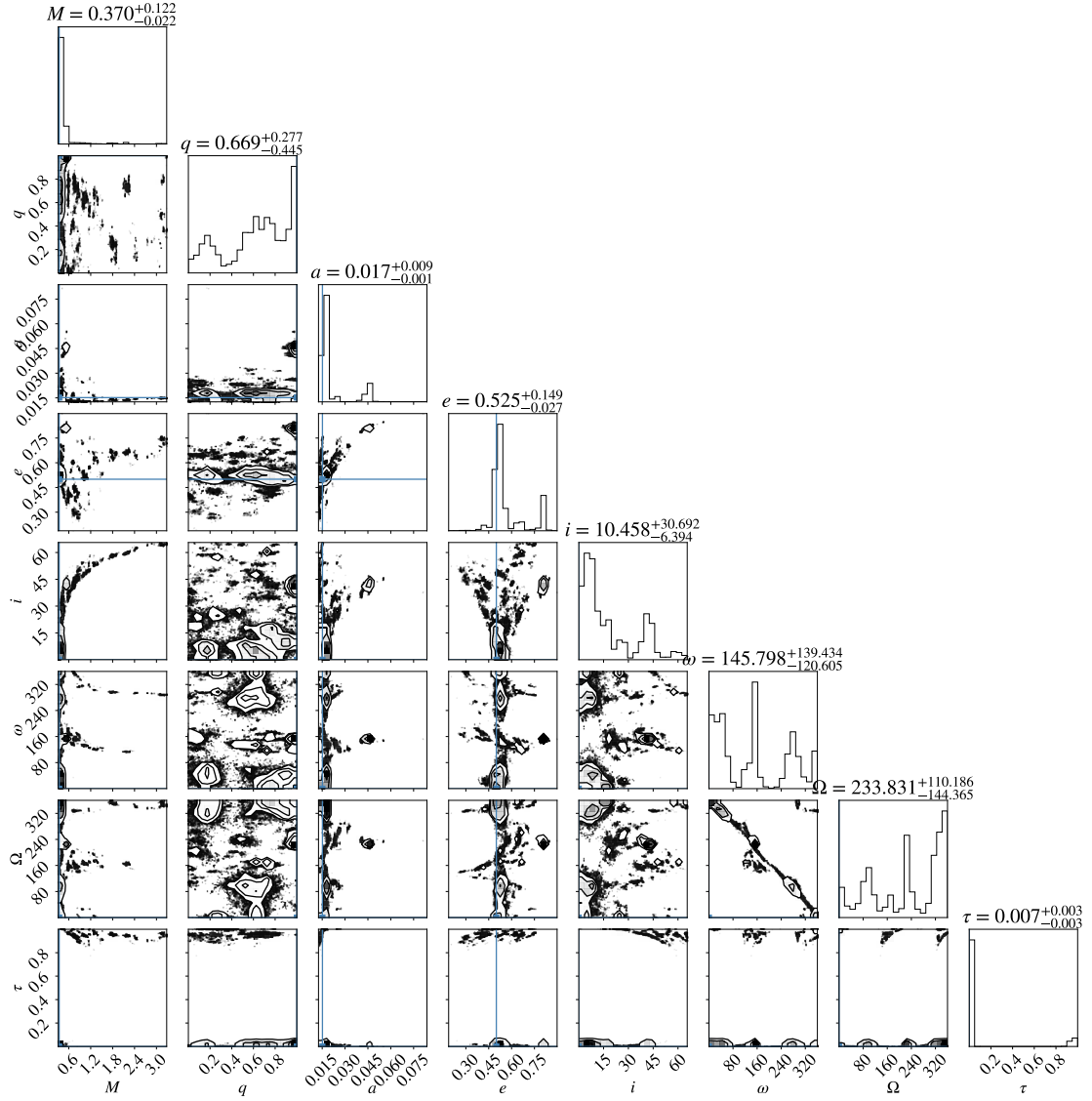


Fig. C.9. Case 2: Corner plot showing posterior distribution.

Table C.4. Case 4 orbit fitting posterior distribution summary. Error between fitted value and true parameter value given in brackets for MAP. Median provided with 68% credible interval ranges.

Parameter	True	MAP	Median
$M [10^9 M_\odot]$	5.62	6.74 (20.0%)	$6.53^{28.0}_{-0.73}$
$q [-]$	0.600	0.353 (41.2%)	$0.470^{0.35}_{-0.44}$
$a [\text{pc}]$	0.0207	0.0215 (3.9%)	$0.0221^{0.013}_{-0.00061}$
$e [-]$	0.000	0.119	$0.156^{0.23}_{-0.12}$
$i [^\circ]$	0.000	27.9	39.6^{120}_{-18}
$\omega [^\circ]$	0.000	87.8	181.0^{120}_{-92}
$\Omega [^\circ]$	0.000	189.2	212.5^{50}_{-180}
$\tau [-]$	0.000	0.810	$0.337^{0.52}_{-0.33}$

Table C.5. Case 5 orbit fitting posterior distribution summary. Error between fitted value and true parameter value given in brackets for MAP. Median provided with 68% credible interval ranges.

Parameter	True	MAP	Median
$M [10^9 M_\odot]$	0.400	0.482 (20.5%)	$0.480^{0.021}_{-0.019}$
$q [-]$	0.060	0.513 (755%)	$0.529^{0.35}_{-0.36}$
$a [\text{pc}]$	0.0101	0.0112 (10.9%)	$0.0110^{0.0012}_{-0.00058}$
$e [-]$	0.000	0.078	$0.068^{0.092}_{-0.045}$
$i [^\circ]$	0.000	27.4	$26.5^{6.5}_{-5.4}$
$\omega [^\circ]$	0.000	12.8	$14.4^{170}_{-7.0}$
$\Omega [^\circ]$	0.000	41.6	$52.5^{170}_{-16.0}$
$\tau [-]$	0.000	0.139	$0.138^{0.034}_{-0.033}$

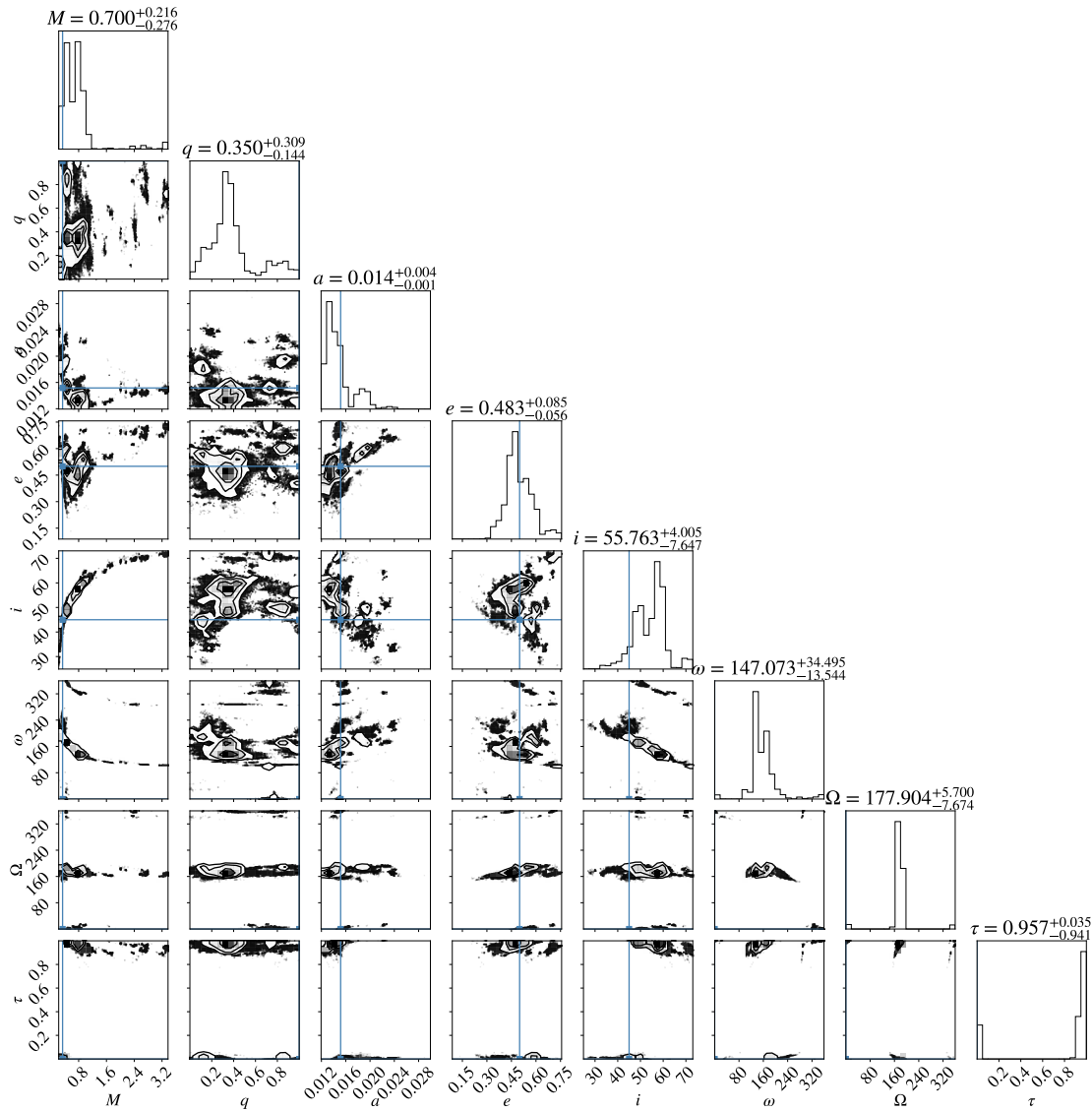


Fig. C.10. Case 3: Corner plot showing posterior distribution.

Table C.6. Case 6 orbit fitting posterior distribution summary. Error between fitted value and true parameter value given in brackets for MAP. Median provided with 68% credible interval ranges.

Parameter	True	MAP	Median
$M [10^9 M_\odot]$	0.337	0.314 (6.9%)	$1.129^{+0.993}_{-0.697}$
$q [-]$	1.000	0.342 (65.8%)	$0.401^{+0.322}_{-0.369}$
$a [\text{pc}]$	0.0152	0.0108 (28.6%)	$0.0121^{+0.00095}_{-0.00088}$
$e [-]$	0.500	0.438 (12.4%)	$0.310^{+0.244}_{-0.253}$
$i [^\circ]$	80	103.9 (29.9%)	$97.4^{+3.6}_{-3.3}$
$\omega [^\circ]$	0	43.7	$136.3^{+116.8}_{-69.0}$
$\Omega [^\circ]$	0	345.0	$172.3^{+178.5}_{-2.38}$
$\tau [-]$	0	0.118	$0.167^{+0.590}_{-0.142}$

Table C.7. Case 7 orbit fitting posterior distribution summary. Error between fitted value and true parameter value given in brackets for MAP. Median provided with 68% credible interval ranges.

Parameter	True	MAP	Median
$M [10^9 M_\odot]$	0.300	0.305 (1.7%)	$0.319^{+0.032}_{-0.020}$
$q [-]$	1.000	0.312 (68.8%)	$0.505^{+0.300}_{-0.342}$
$a [\text{pc}]$	0.0303	0.0304 (0.3%)	$0.0309^{+0.0036}_{-0.0015}$
$e [-]$	0.000	0.00687	$0.0396^{+0.148}_{-0.023}$
$i [^\circ]$	0	4.724	$6.895^{+9.36}_{-4.57}$
$\omega [^\circ]$	0	234.8	$194.0^{+135.5}_{-108.6}$
$\Omega [^\circ]$	0	185.2	$102.4^{+126.6}_{-75.1}$
$\tau [-]$	0	0.164	$0.146^{+0.379}_{-0.116}$

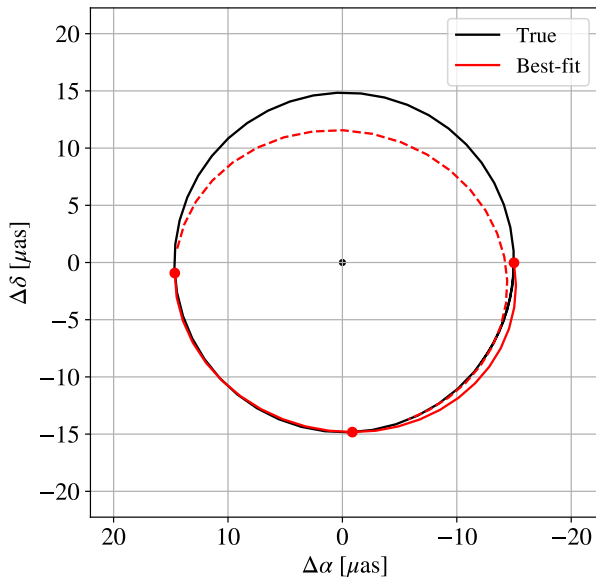


Fig. C.11. Best-fit solution for Case 4. Observed positions of secondary relative to the primary are indicated by red markers with 1σ error bars.

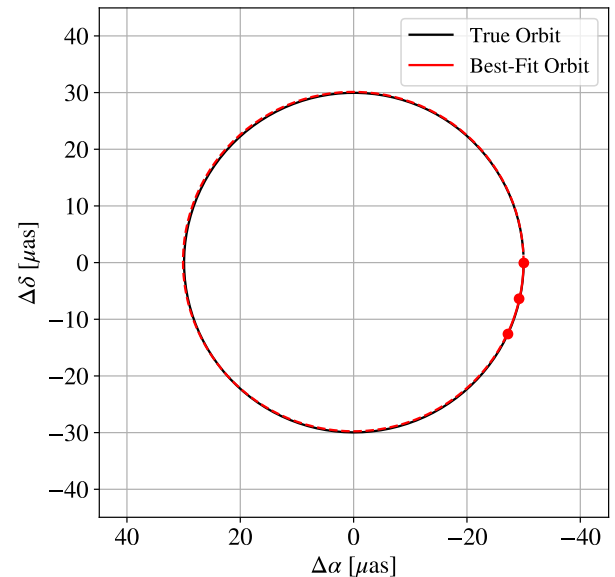


Fig. C.14. Best-fit solution for Case 7. Observed positions of secondary relative to the primary are indicated by red markers with 1σ error bars.

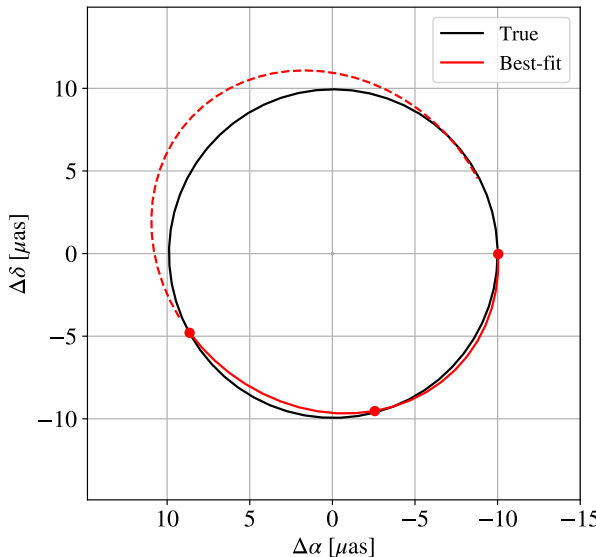


Fig. C.12. Best-fit solution for Case 5. Observed positions of secondary relative to the primary are indicated by red markers with 1σ error bars.

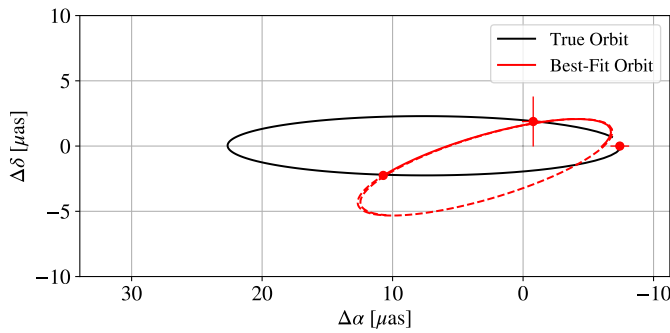


Fig. C.13. Best-fit solution for Case 6. Observed positions of secondary relative to the primary are indicated by red markers with 1σ error bars.